BRNO UNIVERSITY OF TECHNOLOGY

VYSOKÉ UČENÍ TECHNICKÉ V BRNĚ

FACULTY OF MECHANICAL ENGINEERING

FAKULTA STROJNÍHO INŽENÝRSTVÍ

INSTITUTE OF PHYSICAL ENGINEERING

ÚSTAV FYZIKÁLNÍHO INŽENÝRSTVÍ

IN-SITU ANALYSIS OF MAGNETIC PHASE TRANSITION IN FERH USING TRANSMISSION ELECTRON MICROSCOPY

IN-SITU ANALÝZA MAGNETICKÉ FÁZOVÉ PŘEMĚNY V FERH TRANSMISNÍM ELEKTRONOVÝM MIKROSKOPEM

BACHELOR'S THESIS

BAKALÁŘSKÁ PRÁCE

AUTHOR

AUTOR PRÁCE

MARTIN TICHÝ

SUPERVISOR

VEDOUCÍ PRÁCE

Ing. JAN HAJDUČEK

BRNO 2024

BRNO UNIVERSITY OF TECHNOLOGY
FACULTY OF MECHANICAL ENGINEERING

Assignment Bachelor's Thesis

Institut:	Institute of Physical Engineering
Student:	**Martin Tichý**
Degree programm:	Physical Engineering and Nanotechnology
Branch:	no specialisation
Supervisor:	**Ing. Jan Hajduček**
Academic year:	2023/24

As provided for by the Act No. 111/98 Coll. on higher education institutions and the BUT Study and Examination Regulations, the director of the Institute hereby assigns the following topic of Bachelor's Thesis:

In–situ analysis of magnetic phase transition in FeRh using transmission electron microscopy

Brief Description:

Control of magnetic order using external stimuli is pivotal for fundamental research in magnetism and design of low–power magnetic devices. Transmission electron microscopy offers broad possibilities for magnetic order analysis with a spatial resolution below 10 nm. This thesis focuses on in–situ analysis of the phase transition from antiferromagnetic to ferromagnetic order in the FeRh system using a transmission electron microscope.

Bachelor's Thesis goals:

1. Literature review on imaging the FeRh phase transition using TEM.
2. Preparation of planar samples of FeRh for in–situ TEM imaging using selective chemical etching and focused ion beam (FIB).
3. Visualization of the temperature dependence of the magnetic domain structure in prefabricated samples using Lorentz microscopy.

Recommended bibliography:

WILLIAMS, David Bernard a CARTER, C. Barry. Transmission electron microscopy: a textbook for materials science. Second edition. New York: Springer, 2009. ISBN 978-0-387-76500-6.

ALMEIDA, Trevor P.; TEMPLE, Rowan; MASSEY, Jamie; FALLON, Kayla; MCGROUTHER, Damien et al. Quantitative TEM imaging of the magnetostructural and phase transitions in FeRh thin film systems. Online. Scientific Reports. 2017, vol. 7, no. 1, 17835. ISSN 2045-2322. Available at: https://doi.org/10.1038/s41598-017-18194-0.

Deadline for submission Bachelor's Thesis is given by the Schedule of the Academic year2023/24

In Brno,

L. S.

prof. RNDr. Tomáš Šikola, CSc. Director of the Institute	doc. Ing. Jiří Hlinka, Ph.D. FME dean

Summary
Iron-rhodium (FeRh) undergoes a metamagnetic phase transition form the antiferromagnetic to the ferromagnetic phase at a temperature around 370 K. This makes FeRh potentially interesting to many magnetic-oriented branches of industry. One of the techniques, that allows for detailed analysis of both of these magnetic phases is transmission electron microscopy (TEM). This technique is well-known for reaching atomic resolution, but it has many more uses, such as structural, chemical, magnetic and many other types of analysis. However, crucial for any successful TEM measurement is the preparation of samples. Several TEM sample fabrication techniques use focused ion beam (FIB) providing different specimen structural damage and resulting sample geometry. This thesis focuses on imaging the phase transition in FeRh using TEM and assessing the influence of sample fabrication process via FIB on several TEM sample geometries. It was observed that ion irradiation can change or completely remove the phase transition even for doses lower than those used during sample fabrication.

Abstrakt
Železo-rhodium (FeRh) prochází metamagnetickou fázovou přeměnou z antiferomagnetické (AF) do feromagnetické (FM) fáze při teplotě přibližně 370 K. To z FeRh činí potenciálně zajímavý materiál pro mnoho magneticky zaměřených průmyslových odvětví. Jedna z technik, umožňující detailní analýzu obou zmíněných magnetických fázi je transmisní elektronová mikroskopie (TEM). Tato technika je dobře známá díky dosahování atomárního rozlišení, ale má i mnoho dalších použití, jako strukturní, chemickou, magnetickou a mnoho dalších typů analýzy. Nicméně rozhodující pro každou úspěšnou TEM analýzu je výroba vzorků. Několik technik výroby vzorků pro TEM využívá fokusovaného iontového svazku (FIB), což vede k různému stupni strukturního poškození a k různým výsledným geometriím vzorku. Tato práce se zaměřuje na zobrazování fázové přeměny FeRh pomocí TEM a na posouzení vlivu výroby vzorku pomocí FIB na několika různých geometriích vzorku. Bylo pozorováno, že ozáření ionty může změnit nebo kompletně odstranit fázovou přeměnu v FeRh i pro dávky menší než ty používané při výrobě vzorků.

Keywords
iron-rhodium, metamagnetic phase transition, transimission electron microscopy, focused ion beam

Klíčová slova
železo-rhodium, metamagnetická fázová přeměna, transmisní elektronová mikroskopie, fokusovaný iontový svazek

TICHÝ, M.*In-situ analysis of magnetic phase transition in FeRh using transmission electron microscopy.* Brno: Vysoké učení technické v Brně, Faculty of Mechanical Engineering, 2024. ?? s. Vedoucí Ing. Jan Hajduček.

I declare that I have written my bachelor's thesis on the theme of *In-Situ analysis of magnetic phase transition in FeRh using transmission electron microscopy* independently, under the guidance of the supervisor Ing. Jan Hajduček, and usingthe sources quoted in the list of literature at the end of the thesis.

Martin Tichý

First and foremost, I am extremely grateful to my supervisor Ing. Jan Hajduček for his mentoring and patience, continuous support and help with whatever was needed, as well as for many intriguing and inspiring discussions.

I would like to extend my gratitude to the whole *Nanomagnetism* group at CEITEC. Namely I want to thank M.Sc. Jon Ander Arregi, Ph.D. and Ing. Vojtěch Uhlíř, Ph.D. for discussions and many shared insights.

I would also like to recognize the assistance of Ing. Ondřej Man, Ph.D. considering the SEM/FIB system operation.

I cannot thank my family and partner Anežka enough for their encouragement and support at all times.

CzechNanoLab project LM2023051 funded by MEYS CR is gratefully acknowledged for the financial support of both the measurements and sample fabrication at CEITEC Nano Research Infrastructure.

Martin Tichý

Contents

Introduction

The use of magnetic materials has seen a rise in past decades and there are new magnetic-based technologies introduced to the world quite often. Areas that see the incorporation and use of magnetic materials include data storage [31, 39], refrigeration and air conditioning industry [7, 16] or spintronic devices [14, 15, 19, 20]. Such a widening of the use of magnetic materials was made possible by extensive research on magnetic materials, in particular ferromagnets and antiferromagnets.

Ferromagnetic (FM) materials are a traditional branch of magnetic materials that are well understood and easily controllable. However, their theoretical performance is fundamentally limited in data storage density, or magnetization dynamics rate [19].

Antiferromagnetic (AF) materials are another group of magnetically ordered materials, which possess no macroscopic magnetization. Their internal antiparallel alignment of atomic moments allows for potentially higher data storage density and considerably faster dynamics compared to FM materials [20]. However, due to the lack of macroscopic magnetization, the external control and readout of their magnetic state are limited, making them far more challenging for effective use.

Access to both of these magnetic states in one material and a way to activate them would instantly make the material of great interest to many magnetic-oriented branches of industry. One such material, that can be in different magnetic phases depending on external conditions, is FeRh, which is AF at room temperature and with the increase in temperature to around 370 K transitions to FM phase [22].

One of the techniques, that allows for detailed analysis of both AF and FM phase is *transmission electron microscopy* (TEM). This technique is well-known for reaching atomic resolution, but it has many more uses, such as structural, chemical, magnetic and many other types of analysis [2, 17, 42]. The challenge remains in probing the phase transition, due to invasive sample fabrication process required for TEM investigation. Several approaches of TEM sample fabrication have been historically developed providing different specimen structural damage, resulting geometry, and fabrication process convenience [42]. The most heavily used one includes using Focused Ion Beam (FIB), that is highly invasive in particular for FeRh [1].

This thesis is focused on imaging the phase transition in FeRh using TEM and quantitatively assess the influence of FIB on FeRh phase transition properties in multiple different sample geometries.

This thesis is divided into 4 chapters. Chapter 1 briefly covers the basics of nanomagnetism and magnetic ordering of solids. Chapter 2 introduces FeRh and provides information about its properties, phases and phase transitions. Chapter 3 is dedicated to the general principles of TEM and briefly covers the TEM setup and its operation modes. Finally in chapter 4, we discuss the experimental results of the thesis.

1. Basics of nanomagnetism

Deep understanding of the physical processes in magnetic materials starting from the nanoscale up to the macroscale is essential for potential applications of magnetic materials. In this chapter, we briefly touch upon the origins of magnetic properties in solids. A detailed description of these phenomena is widely covered in multiple magnetism theory-related books [9, 11], therefore only a summary is presented. First, we define the magnetic moment and with it the magnetization, which we then connect with magnetic field. We then divide materials according to their internal magnetic ordering and finish with phase transitions between different types of magnetic ordering.

1.1. Magnetic moment

The elementary quantity in magnetism is the magnetic moment. In classical electromagnetic theory we can equate this with a current loop. If there is a current around an oriented loop of area $|\mathrm{d}\mathbf{S}|$ then the magnetic moment $\mathrm{d}\mu$ is given as

$$d\mu = I\mathbf{dS}, \tag{1.1}$$

the SI unit of which is $\mathrm{A/m^2}$. The length of the vector $\mathrm{d}\mathbf{S}$ is equal to the area of the loop and the direction of the vector is normal to the loop and is determined by the direction of the current around the loop.

For a loop of finite size, we can calculate the magnetic moment μ by summing up the magnetic moment distributed throughout the area of the loop,

$$\mu = \int I dS. \tag{1.2}$$

A current loop occurs because of the motion of an electrical charge, equal to the motion of a charged particle. Magnetic moment is therefore connected with the angular momentum of the particle.

In magnetic atoms the magnetic moment μ associated with an orbiting electron connects with the angular momentum L of that electron, hence

$$\mu = \gamma L, \tag{1.3}$$

where γ is a constant called gyromagnetic ratio. As the charge of an electron is negative, its magnetic moment is antiparallel to its angular momentum.

Magnetic matter consists of atoms with magnetic moments. The magnetization $\mathbf{M}$ of a solid is defined as the sum of magnetic moments μ per unit volume V:

$$\mathbf{M} = \frac{\sum_i \mu_i}{V}, \tag{1.4}$$

the SI unit of which is A/m.

1.2. Magnetic field

Maxwell equations describe electromagnetic field distributions, and one of them, the Gauss law of magnetism, is written as:

$$\nabla \cdot \mathbf{B} = 0, \tag{1.5}$$

where $\mathbf{B}$ is divergence-less, implying the nonexistence of magnetic monopoles and gives us another way of expressing $\mathbf{B}$ as

$$\mathbf{B} = \nabla \times \mathbf{A}, \tag{1.6}$$

where $\mathbf{A}$ is the magnetic potential vector.

Interaction of charged particles with a magnetic field is the key for analysis and imaging of magnetic materials, but $\mathbf{B}$ interacts with charges only when they move. This interaction is in classical mechanics described in terms of the Lorentz force as:

$$\mathbf{F} = q\mathbf{v} \times \mathbf{B}, \tag{1.7}$$

where q is the particle's charge and $\mathbf{v}$ its velocity.

Another approach of describing the magnetic field is through the $\mathbf{H}$-field. In free space (vacuum) there is no magnetization. The magnetic field can therefore be described by the vector fields $\mathbf{B}$ and $\mathbf{H}$ which are linearly related as:

$$\mathbf{B} = \mu_0 \mathbf{H}, \tag{1.8}$$

where μ_0 is the permeability of vacuum.

However, in magnetic materials the relation between $\mathbf{B}$ and $\mathbf{H}$ can be more complicated as the two field vectors may not be collinear. The general relationship in this case is:

$$\mathbf{B} = \mu_0(\mathbf{H} + \mathbf{M}), \tag{1.9}$$

and the $\mathbf{H}$ and $\mathbf{M}$ fields are connected by the magnetic susceptibility, written as

$$\mathbf{M} = \chi \mathbf{H}, \tag{1.10}$$

where χ is magnetic susceptibility [9, 11].

1.3. Magnetic ordering

There are 3 (4) basic types of magnetic ordering in solid materials - *diamagnetism*, *paramegnetism*, *ferromagnetism* and *antiferromagnetism*. As the first one is not relevant to this work, we will focus only on the rest.

1.3.1. Paramagnetism

Paramagnetism (PM) corresponds to a state of material, such that the magnetic moments of individual atoms point in random directions, hence their effects cancel out and the total magnetization of the whole object is 0. This type of magnetic ordering can be seen in Figure 1.1 (a). When a magnetic field is applied, it orients the magnetic moments in its direction, inducing magnetization parallel with the applied magnetic field, represented in Figure 1.1 (b) [9, 11].

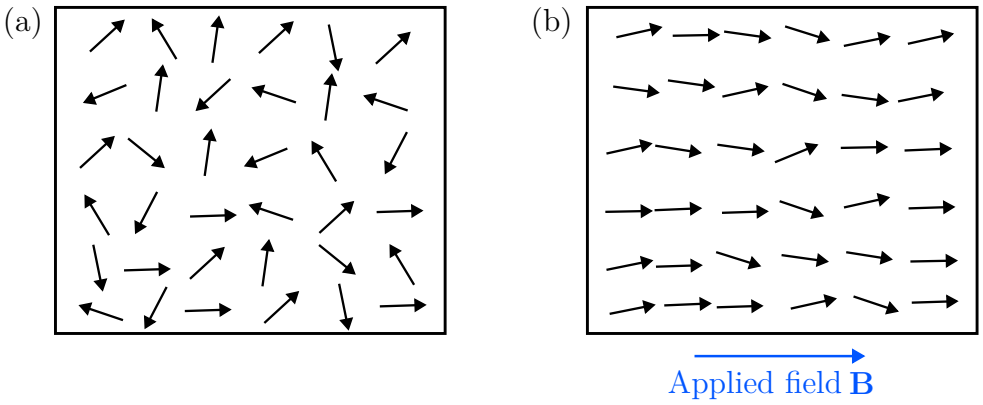

Figure 1.1: (a) Scheme of the paramegnetic ordering without applied magnetic field. The magnetic moment of each atom has a different random orientation, independent on the orientation of other nearby magnetic moments. (b) Scheme of the paramagnetic ordering while field is applied. Magnetic moments are tilted in the direction of the field. At zero temperature, they would be parallel, but in usual conditions, they are not entirely parallel due to thermal oscillations.

1.3.2. Ferromagnetism

Another type of magnetic ordering is called ferromagnetism (FM). A FM material is characteristic for its spontaneous magnetization M_s even in the absence of an applied magnetic field. This magnetization is present due to the alignment of magnetic moments on the atomic scale originating from exchange interaction, which can be seen in Figure 1.2 (a). An essential feature of a FM material is the dependence of magnetisation on applied magnetic field, which has the form of a hysteresis loop, an example of which can be seen in Figure 1.2 (b). If the material is magnetized by an external magnetic field to the saturation magnetization M_s, when the external magnetic field is reduced to zero, the magnetization lowers to remanent magnetization M_r. The coercive field H_C corresponds

to the points in the hysteresis where magnetization is 0 [9, 11].

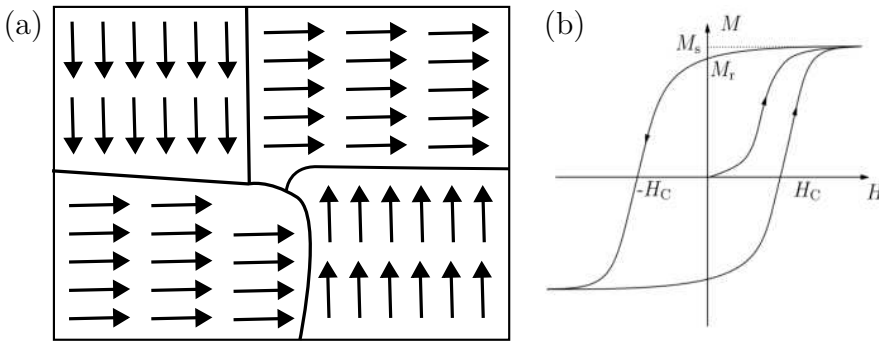

Figure 1.2: (a) Scheme of the ferromagnetic ordering. The material is broken into magnetic domains, in which all magnetic moment have the same orientation. (b) A prototypical hysteresis loop. M_s denotes the saturation magnetization, M_r is the remanent magnetization when an applied magnetic field is switched off and H_C is the coercive magnetic field, which corresponds to the points in the hysteresis where magnetization is 0. Adapted from [11].

1.3.3. Antiferromagnetism

The magnetic moments of atoms in an antiferromagnetically (AF) ordered material are oriented antiparallel to their nearest neighbours. This can also be decribed as the material having two magnetic sublattices, oriented in the opposite direction. A schematic of this magnetic ordering is represented in Figure 1.3 (a). In this orientation, the magnetic moments cancel out, resulting in zero net magnetization. Applying a magnetic field to an antiferromagnet, shown in Figure (b), creates much more complicated results than in the case of a paramagnet. All magnetic moments try to orient themselves along the applied field, their respective antiparallel orientation combined with magnetic anisotropy make the overall magnetic state complex. [9, 11].

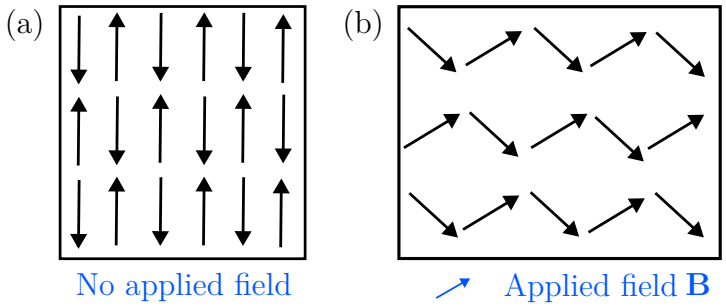

Figure 1.3: Scheme of the antiferromagnetic ordering. (a) Without applied megnetic field, magnetic moments of neighbouring atoms are antiparallel, but have the same magnitude. (b) Field applied parallel to the orientation of magnetic moments has to effect. (c) Field applied perpendicular to the orientation of magnetic moments tilts them in the direction of the applied field.

1.4. Magnetic phase transitions

If a material is in one of the above mentioned magnetic states, it does not mean it stays like that in all circumstances. Any material with fixed chemical composition has multiple material states, called "phases", and in the right conditions, it can transition form one phase to the other through a process called "phase transition" (PT). There is a number of magnetic PTs, some of which are PT occurring at the *Neél point*, when an antiferromagnet changes into paramagnet, Pt occurring at the *Curie point*, when a ferromagnet changes into paramagnet or a metamagnetic PT (MPT). The latter two are important for this work and will be shortly described below.

PTs are categorized depending on the order parameter that changes throughout the transition. A "first-order PT" is characterized by discontinuity in the first derivative of the material's free energy, which manifests as a sharp change in the order parameter. A "second-order PT" does not include this discontinuity, which corresponds to a continuous change in the order parameter. In case of magnetic PTs, the order parameter is magnetization.

Some materials have a so-called "Curie temperature" T_{C}, at which a second-order PT from the FM to the PM phase of material occurs. Some examples are Fe ($T_{\mathrm{C}} = 1050$ K), Ni ($T_{\mathrm{C}} = 630$ K) or Co ($T_{\mathrm{C}} = 1400$ K, highest known).

MPT is a type of first-order PT, induced by temperature or applied magnetic field. As a first-order PT, the MPT exhibits a sharp change in magnetization. This effect appears in materials that undergo the transition from the AF to the FM phase, and is present due to the stabilization the applied external stimulus lends to the FM phase [9, 11, 32, 33].

2. FeRh

Near-equiatomic iron-rhodium (close to $Fe_{0.5}Rh_{0.5}$) undergoes a first-order magnetostructural phase transition from antiferromagnetic (AF) to ferromagnetic (FM) phase close to room temperature (upon heating to around 350 K) [13, 22, 41]. This first-order phase transition exhibits a thermal hysteresis, accompanied by a lattice parameter change of about 0.3 % and a change in magnetization [22, 38]. Its combined magnetic and structural propperties make FeRh a very interesting material for theoretical study of the phase transition. The changes the transition brings upon the system are of great interest for technological applications too, such as heat-assisted magnetic recording (HAMR) devices [31, 39], magnetocaloric microsystems [7, 16] or spintronics [14, 15] and antiferromagnetic spintronics [20].

2.1. Crystalline structure and phase transition

The magnetostructural phase transition occurs only in a narrow range of possible compositions from $Fe_{48}Rh_{52}$ to $Fe_{54}Rh_{46}$, as can be seen from Fe-Rh phase diagram shown in Figure 2.1. Even in such a narrow range of composition percentages, these slight deviations have a big effect on the transition temperature, lowering it with decreasing Rh part. The grain size of the material also changes significantly, increasing from hundreds to thousands of Å with a decrease in Rh [28, 38, 44].

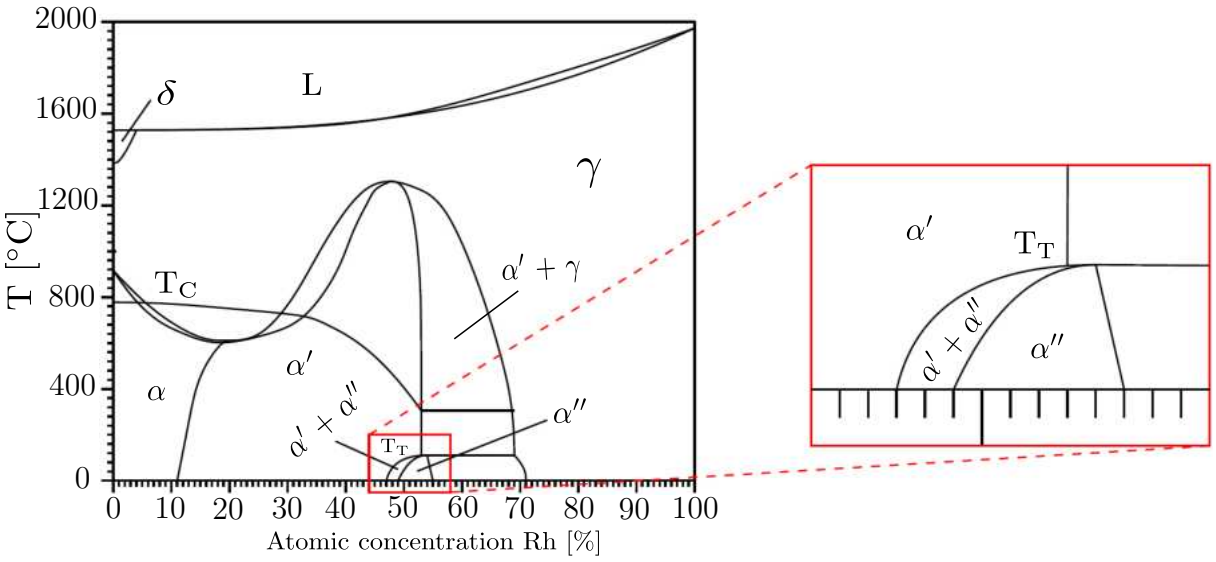

Figure 2.1: FeRh phase diagram, and zoomed-in region of interest of the phase diagram: L - liquid phase; γ- paramagnetic FCC phase; δ- high temperature BCC phase; α- low temperature BCC phase; α' - FM FeRh phase with CsCl-type structure; α" - AF FeRh phase with CsCl-type structure; T_C is the Curie temperature curve and T_T is the transition temperature. Adapted from [38].

Below the phase transition temperature T_T, FeRh behaves as a conventional AF material, while above the transition temperature T_T as a conventional FM. By increasing the

temperature to the Curie point T_C of about 675 K, it undergoes a second-order transition from FM state to paramagnetic (PM) state. [22, 38, 41, 44]

The transition being "first-order" means that the change from AF to FM phase (and reverse) is not immediate and exhibits thermal hysteresis and coexistence of both phases. As the system is heated to T_T, ferromagnetic domains begin to nucleate in the AF material, and this continues until the maximum magnetization is reached, and the sample becomes completely ferromagnetic. It is the same with cooling, only with AF domains nucleating in the FM bulk until the minimum magnetization is reached, when the sample becomes completely antiferromagnetic [25, 30].

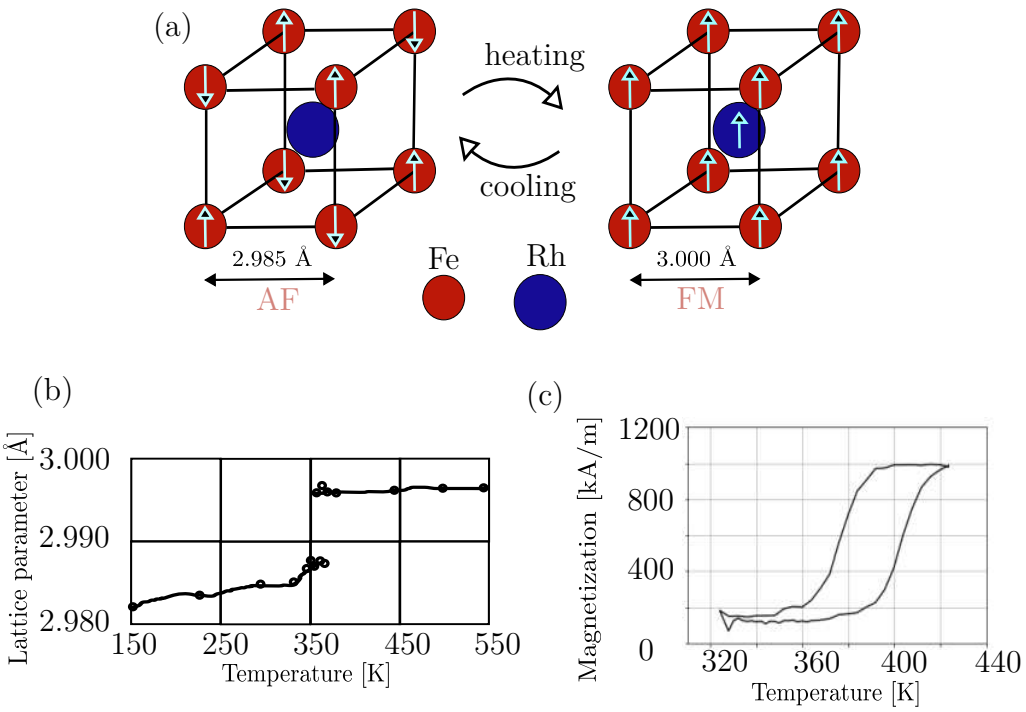

Figure 2.2: (a) The lattice structure of FeRh, with a noted orientation of magnetic moments and lattice parameters in each phase. (b) The temperature dependence of FeRh lattice parameter, adapted from [44]. (c) The temperature dependence of magnetization in thin FeRh film, indicating the presence of AF and FM phases. Measured by Vibrating Sample Magnetometry (VSM).

FeRh is especially remarkable for its very symmetric crystal structure and simple chemical composition. It has a simple cubic lattice of Fe intertwined with a simple cubic Rh lattice, where the corner of one cell is the center of the body of the other cell. This arrangement is called the CsCl-type structure, and is usually viewed as a body-centered cubic (BCC) lattice, in which Fe atoms occupy the outer corners of the cubic unit and the Rh atom is in the middle position, as shown in Figure 2.2 (a). [23, 38, 41] This crystalline structure is retained throughout the transition, only with a slightly increased lattice parameter, from 2.987 Å in the AF phase at room temperature to about 3.00 Å in the FM phase [25, 38, 44].

While antiferromagnetic, Fe atoms have a magnetic moment of 3.3 μ_B, with the moments of nearest-neighbour Fe atoms being antiparallel (pointing in opposite directions), and they switch to being parallel in the FM state with the size of the moments lowering to 3.2 μ_B. Meanwhile, Rh atoms have no detectable magnetic moment in the AF state, which changes to 0.9 μ_B in the FM state with the same orientation as the nearest Fe atoms [23, 25, 34].

2.2. Phase transition tunability

The phase transition results in simultaneous changes in both the magnetic and structural properties, and can be induced by temperature, applied magnetic fields, strain, or doping with other elements. [23] Increasing the temperature of the system to the transition temperature T_T is the most often used way of triggering the phase transition, with other above-mentioned factors applied to lower that temperature [22, 38, 41, 44]. More detailed description of individual factors follows below.

Doping bulk FeRh with small amounts (a few atomic %) of Pt, Ru, Ir and Os increases the transition temperature, while additions of Pd, V, Mn, Au, Al,Cr, Ni or Cu move the transition temperature to lower values. It should be noted that there is a limit to how much of those elements can be added to affect the transition temperature, but not remove it completely. For those elements increasing the transition temperature, additions of more than 5 % usually completely eradicate the FM phase and the system transitions directly to PM upon reaching the Curie temperature, while for too much of elements decreasing the transition temperature, the system remains in the FM phase even close to 0 K. There are also some elements, namely Co, Nb, Mo, Ta and W, which eliminate the transition altogether with as little as 2 atomic % [6, 21, 23, 40, 41].

Subjecting FeRh to magnetic field stabilizes the FM phase, which decreases the transition temperature at a rate of about $-8.2\ \mathrm{K} \cdot \mathrm{T}^{-1}$. By extrapolation, this gives us a value of around 6 T to fully induce the transition at room temperature just by applied magnetic field [25, 26, 38].

The increase of pressure has a profound effect on the T_T both on heating and cooling, increasing it approximately linearly by a value of 4.3-6.3 K/kbar, but it has another effect, which is a slight decrease in T_C of about 0.6 K/kbar. If these values do not change with increasing pressure, we then get a so called "tripple point" at around 56 kbar, where the first-order transition disappears and only the second-order transition to PM phase remains [38, 41, 44].

Crystallographic ordering of FeRh also has a huge effect on the transition. Most of the studied FeRh samples had been annealed for different lengths of time and many researchers had observed the effects these differences (or the lack of annealing at all) had on the system. As-made FeRh samples reveal a significant amount of FCC phase, most of which changes to CsCl-type structure as a result of annealing. One thing became clear quite soon, and that is that the longer the annealing continues, the better the inhomo-

geneities in composition and lattice structure diffuse, and the ordered CsCl-type structure symmetry is expanded throughout the sample, and with this increasing symmetry, the transition temperature gets lower. However, the remaining FCC phase and compositional inhomogeneities, which usually have a different orientation than the ordered CsCl-type structure, and defects in the crystalline structure play a significant role in preventing a narrow and complete transition and stabilize the FM phase [21, 24, 28, 38].

Another factor that can influence the transition temperature of FeRh is controlled ion irradiation, which on purpose induces defects in the system. Low ion doses lower the transition temperature and increase magnetization, but the dose needed to induce the transition depends on used ion type. To fully induce the transition at room temperature, a dose of He^+ or H^+ ions of around 10^{15} cm^{-2} is needed, with this dose lowering for heavier ions (such as Ga^+ or Ne^+) to about 10^{13} cm^{-2}. The effects of irradiation with H^+ and He^+ ions can be seen in Figure 2.3 (a) and (b) respectively. If the sample is irradiated more, the FM α" phase starts transforming into the PM γ phase, the material essentially undergoing the second-order FM $\rightarrow$ PM transformation [1, 8, 18, 35].

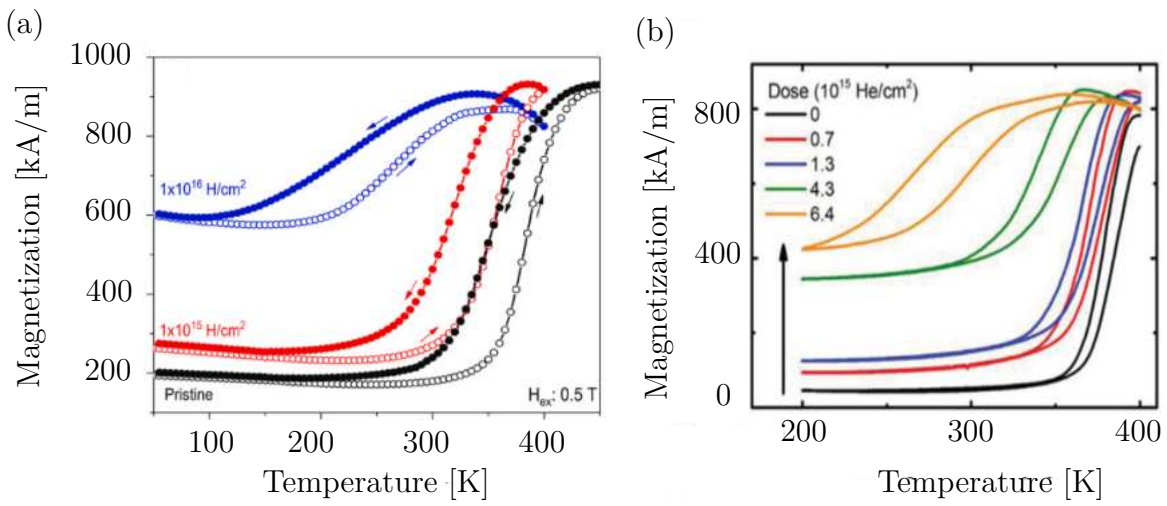

Figure 2.3: Effect of (a) H^+, (b) He^+ ion irradiation on FeRh phase transition properties. Gradual shift to lower temperatures and increased residual FM portion in AF phase are apparent with growing dose. Adapted from [35] and [8] respectively.

2.3. Properties of FeRh thin films

Thin film versions of FeRh exhibit magnetic and structural characteristics that align with those observed in bulk FeRh, such as the AF to FM transformation accompanied by lattice expansion upon heating and the effect dopants and magnetic field have on the transition temperature.

The differences, however, are quite intriguing. The compositional range, in which the transition occurs increases slightly on both sides (for rhodium part from [46 - 52]% to [45.4 - 54]%) and magnetization at room temperature decreases continuously in contrast

to the sharp drop at equiatomic composition in bulk. The transformation also is not abrupt as in bulk, but is quite gradual with AF and FM parts existing at the same time, and the thermal hysteresis of the transformation gets much broader [24, 28, 29].

Thin films are epitaxially grown on substrates, but as those substrates are a different material, they have different lattice parameters. This lattice mismatch induces strain in the film, which affects the T_T, with the degree of the response depending on the thickness (a few hundred nm for thickest films up to few nm for very thin ones) of the film.

The most common among the substrates used for FeRh growth are MgO (001) and Al_2O_3 (0001) (sapphire). Figure 2.4 (a) shows that on MgO(001) substrate, FeRh grows in the (001) orientation, which is rotated 45° with respect to the substrate, and Figure 2.4 (b) shows that on sapphire substrate, FeRh grows in the (111) orientation. On MgO, the FeRh film is slightly compressed in-plane and expands out-of-plane (tetragonal distortion), while on sapphire the film is expanded in-plane and compressed out-of-plane (trigonal distortion). Exact values of induced strain can be found in Table 2.1. Even though the lattice parameters are slightly changed, the volume of a structural cell is roughly the same. As FeRh has a smaller lattice parameter in the AF phase and larger in the FM phase, it can be expected that MgO substrate (which compresses the film in-plane) will stabilize the AF phase, and oppositely sapphire substrate (which causes an expansion in-plane) will stabilize the FM phase, increasing and decreasing the transition temperature respectively, as shown in Figures 2.4 (c) and (d) [25].

Table 2.1: Lattice and strain parameters of FeRh films grown onto MgO(001) and Al_2O_3(0001). Strain values are derived from the bulk FeRh lattice parameter of 2.987 Å. Reproduced from [25].

Orientation		[Å]	Strain [%]	[Å]	Strain [%]
FeRh/MgO	FeRh/Al_2O_3	FeRh/MgO	FeRh/MgO	FeRh/Al_2O_3	FeRh/Al_2O_3
(002)	(111)	2.9980	+0.33	2.9800	-0.27
	(110)			2.9854	-0.09
(011)		2.9890	+0.03		
	(200)			2.9901	+0.07
(020)	(110)	2.9750	-0.44	2.9950	+0.23

Other used substrates for FeRh growth include materials such as W, $KTaO_3$ (KTO) or $SrTiO_3$ (STO). W(001) promotes the FeRh lattice growth similar as on MgO. Its lattice parameter of 3.165 Åresults in strong tensile strain on FeRh, hence reducing the FeRh transition temperature [4]. $KTaO_3$ and $SrTiO_3$ substrates induce compressive strain, which results in increasing the FeRh transition temperature [4, 10, 25].

As mentioned above, the thickness of the FeRh thin film with respect to the substrate is another parameter, that affects the magnetostructural transition through the strain relaxation properties. Figure 2.5 shows that for thicknesses in the order of hundreds to tens of nm, the film behaves like bulk (with respect to the effect of substrate), but with film thickness crossing a line around 20 nm, the stability of the FM phase rapidly increases,

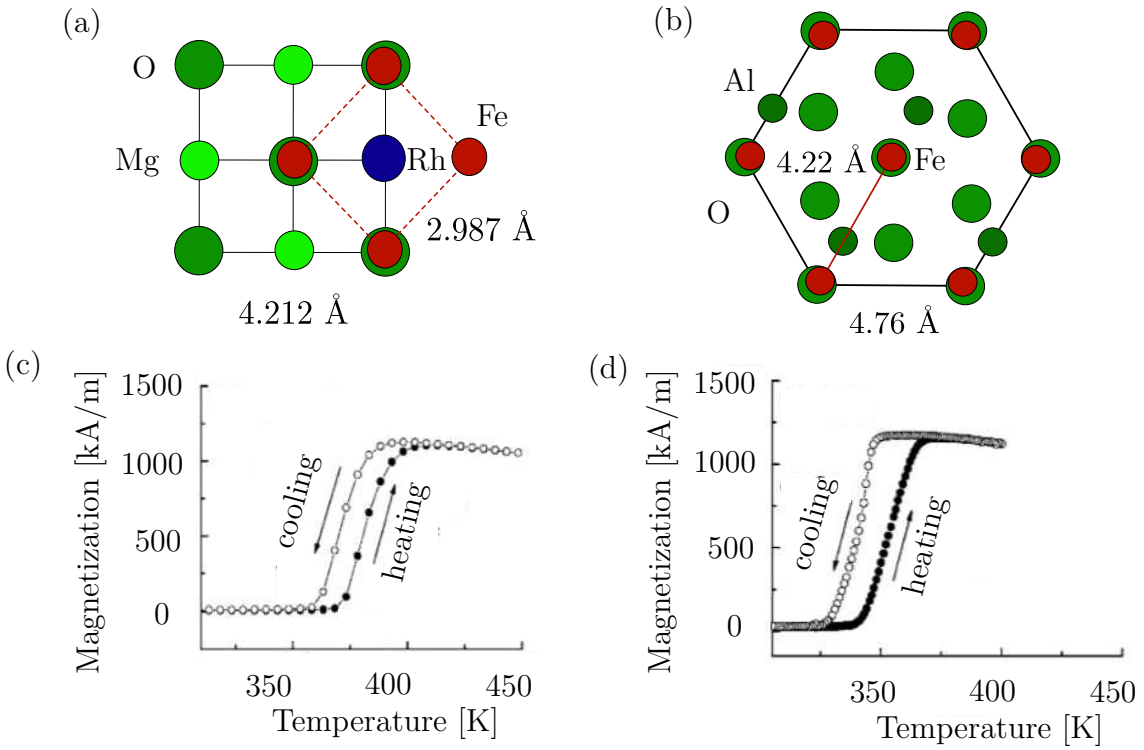

Figure 2.4: (a) Lattice mismatch scheme for FeRh on MgO substrate. (b) Lattice mismatch scheme for FeRh on Al_2O_3. (c) FeRh phase transition on MgO. (d) FeRh phase transition on Al_2O_3. Schematics adapted from [4], phase transition graphs adapted from [25].

lowering the transition temperature [10, 37].

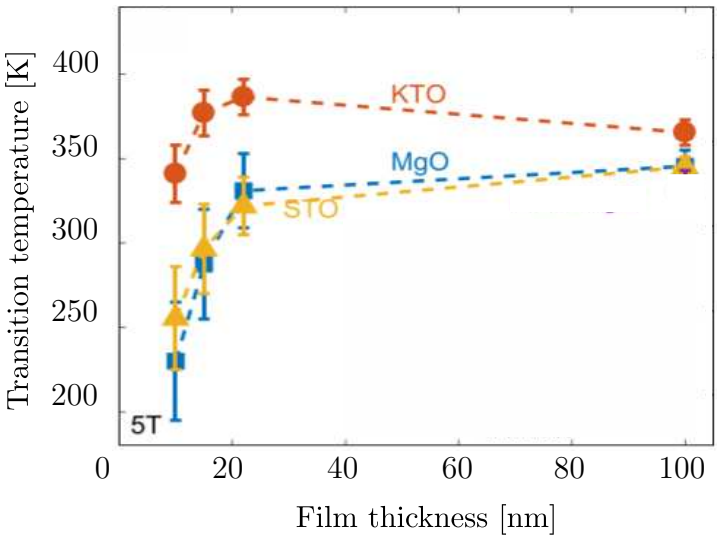

Figure 2.5: The effect of FeRh film thickness on the transition temperature for different substrates. Adapted and edited from [10].

3. FeRh phase transition imaging methods in TEM

The phase transition in FeRh has been observed by many different techniques. Among the most conventionally used are optics-based methods, utilizing the magnetooptical Kerr effect (MOKE) [4]. Other methods include X-ray magnetic circular dichroism (XMCD) [5], magnetic force microscopy (MFM) [43], scanning electron microscopy with polarization analysis (SEMPA) [45], and transmission electron microscopy (TEM) [2, 3, 17]. The resolution of optical methods is limited to hundreds of nm by the use of visible light. In the case of SEMPA, MFM and XMCD, their resolution limit is much lower, but still in the tens of nm. TEM surpases them by the use of high-energy electrons to reach atomic resolution.

In this work, we used the TEM for the reasons mentioned above - very high spatial resolution coupled with the potential for changing the temperature of the sample without affecting the measuring process or the machine itself.

The TEM, being a complicated and finely tuned system, allows for for many different types of sample analysis. Therefore, the list of possible TEM techniques and different properties measurable by them is long and growing still. In this chapter, we will describe the construction and working modes of the TEM, highlighting those important for our work. We will then conclude with the state of the art of TEM phase transition imaging.

3.1. Transmission electron microscope

The basic working principle of TEM is the passing of high-energy electrons through a sample, and detecting the changes in both the energies and trajectories of those electrons, as well as detecting other signals created by the passage of electrons through the sample, such as emitted secondary electrons or x-rays.

The TEM is a very precisely tuned setup, consisting of many components such as electron-optical lenses, aberation correction elements, various detectors etc. These can be broadly divided into three segments - an *illumination system*, *objective/stage system* and *imaging system*. More detailed description follows, and a schematic of the system can be seen on Figure 3.1.

The illumination system can be divided into an *electron source* and a *condenser system* and the imaging system can be divided into a *projection part* and a *detection part*.

The *electron source* consists of an electron gun, a high-voltage accelerator and optionally a monochromator. The electron gun produces an electron beam which is then accelerated by a high-voltage anode to energies usually between 60 and 300 kV, with the monochromator helping to reduce the energy dispersion of the beam.

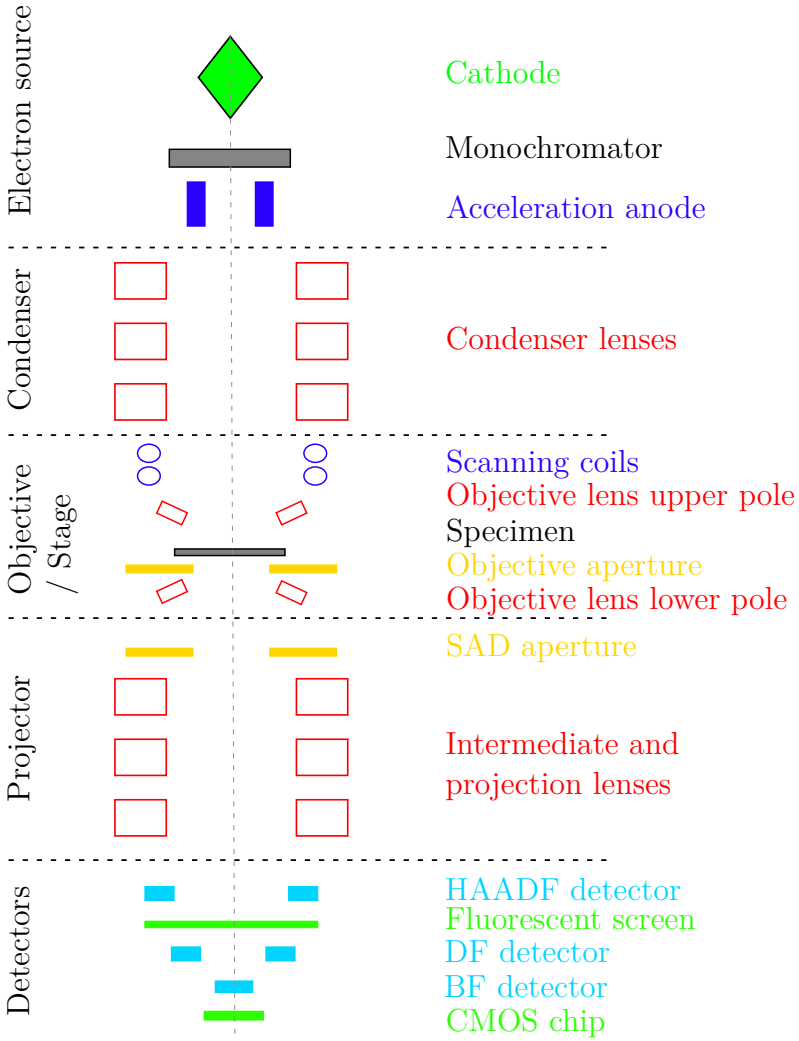

Figure 3.1: Schematic of the TEM building blocks. The system is divided into 5 main parts - the electron source, condensers, objective/stage system, projector and detection part. Closer description of each part in provided in the text above and below.

The *condenser system* consists of a number of condenser lenses, most often 2 or 3. Its function is to adjust the beam diameter, convergence angle, and the electron current. It can be followed by a probe corrector to negate the various optical aberrations of the condenser lenses.

The *objective/stage system* includes the objective lens, scanning coils and the specimen. The scanning coils enable the scanning in the *scanning TEM* (STEM) mode. Many other parts can be present, such as a microcondenser to enhance the efects of the *condenser system*, the Lorentz lens for magnetic imaging and image correctors.

The *projection system* consists usually of 4 lenses, and its main purpose is to magnify the image produced by the objective lens. We can also produce diffraction patterns of the sample by focusing the lenses is such a way, that the object plane of the first projection lens is in the back focal plane (BFP) of the objective lens.

The *detection system* serves for data acquisition. A fluorescent screen, recorded by a camera serves to visualize the magnified beam. High-resolution acquisition is then performed using CMOS chip located below other detectors. Electrons scattered in STEM mode are collected with the bright field, dark field and high angle annual dark field detectors [42].

3.2. TEM imaging modes

In this section we will briefly describe some of the most conventional TEM modes, and those that are important for our work.

There are two modes for beam settings - the *parallel beam* and the *convergent beam*, and two modes for imaging settings - the *imaging mode* and the *diffraction mode*, to choose from when working with TEM.

Parallel beam in the imaging mode is also known as *conventional* TEM (CTEM) and in the diffraction mode, we talk about the parallel diffraction mode, or *selected area electron diffraction* (SAED). The parallel beam mode often utilizes the objective and selected area diffraction (SAD) aperture, which are located in the objective BFP and the image plane, respectively. The objective aperture cuts the spatial frequencies of the diffraction pattern formed in the objective BFP, allowing for BF or DF imaging, while the SAED aperture spatially limits the region from which the diffraction pattern is formed.

The convergent mode is operated practically mostly in the diffraction mode, in which *convergent beam electron diffraction* (CBED) and STEM imaging can be done, while the imaging mode is used mainly for optical alignment of the TEM. STEM utilizes the signal taken from a spatially localized region for all kinds of spectroscopies available in TEM [42].

3.2.1. Magnetic imaging techniques

The following text describes selected approaches for magnetic imaging in TEM, namely *Differential phase contrast* and *Fresnel Lorentz TEM*. It is important to note that magnetic imaging techniques do not have as high resolution as classical BF TEM imaging, detecting magnetic details on a scale of 5 nm. [Chapman]

Differential phase contrast (DPC) is a STEM technique based on the detection of the deflection of the electron beam, which comes from the internal electric or magnetic fields of the sample. On a segmented detector, we can then compare signals from multiple segments to evaluate the deflection of the electron beam by the sample internal magnetic field.

Lorentz TEM (LTEM) is a kind of magnetic phase contrast imaging, which uses the Lorentz lens instead of the objective lens to visualize magnetic signal from the sample. LTEM itself has two modes - the *Foucault* imaging and the *Fresnel* imaging. Both are represented in Figure 3.2. In the Fresnel variant, by defocusing the electron beam, we can visualize magnetic domain walls, which appear as alternating black and white lines.

In the Foucault variant, we can visualize magnetic domains by displacing the objective aperture. In this work, we used the Fresnel variant [42].

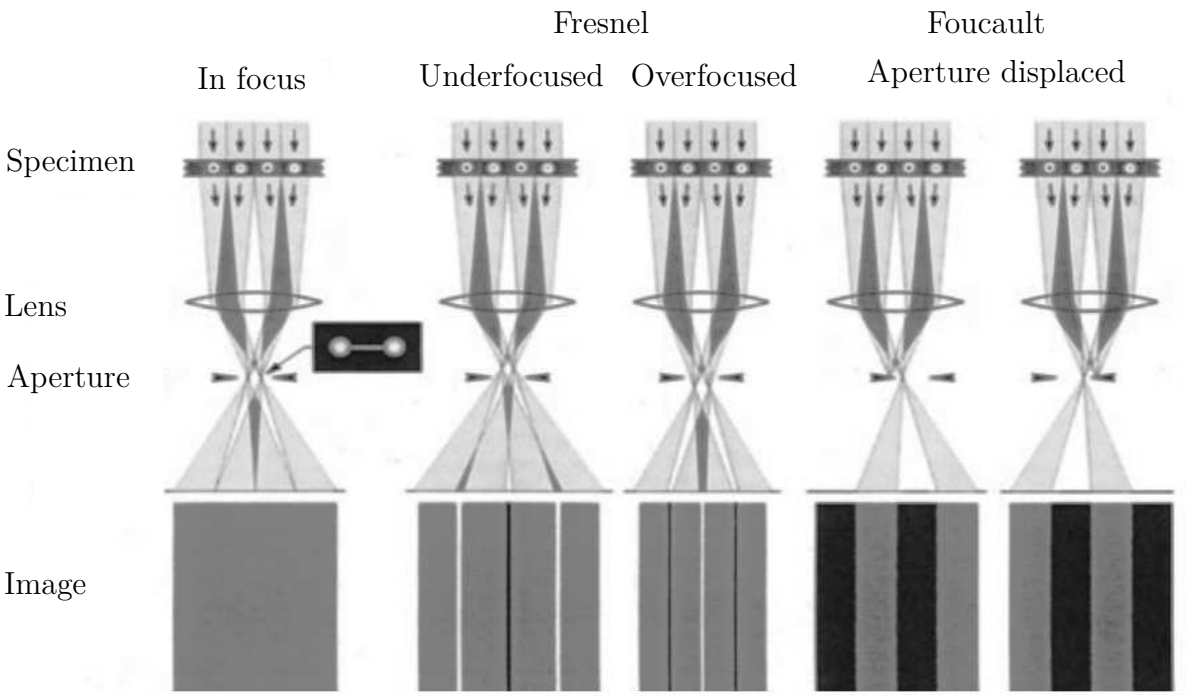

Figure 3.2: Schematic of the two variants of Lorentz TEM imaging mode - Fresnel, which visualizes magnetic domain walls by defocusing the electron beam, and Foucault, which visualizes magnetic domains by displacing the objective aperture [36].

3.3. State of the art of FeRh phase transition imaging in TEM

TEM has been used to observe the phase transition in FeRh in recent years. Gatel and coworkers [17] observed the phase transition in a cross-section lamella using electron holography. They found, that the interfaces between the FeRh film and substrate and between the film and the capping layer were FM at room temperatures and with increasing temperature, the FM phase expanded from those areas to the whole film. They observed that the interfaces not only lower the transition temperature but also widen the transition hysteresis considerably.

In the same year, Almeida and coworkers [3] observed the nucleation process of domains in planar and cross-section samples using DPC, at different temperatures and with varying visibility for different sample fabrication processes. They concluded that using FIB for TEM sample fabrication changes the material by introducing structural disorder and strong shape anisotropy from its original thin film form, with varying degrees of change for different substrates. Additionally, it was shown that post-fabrication annealing can restore some of the FIB-induced disorder. From all their samples, the phase transition

was most clearly observed in a planar film chemically detached from the substrate.

A few years later, Almeida and coworkers expanded their research approach with a novel technique called 4D STEM DPC[1], which allowed them to achieve even better spatial resolution, reaching nm-scale detail [2]. They mapped the phase transition closely and observed the domain nucleation process and expansion. They also confirmed their previous observations, that the substrate-film interface acts as a strong FM domain nucleation center and that sample fabrication via FIB changes the transition significantly.

In most of these cases, a lowering in transition temperature in the samples compared to bulk FeRh was observed. This can be explained by spatial confinement coupled with strain relaxation, interface effects and FIB-induced damage in the case of a lamella, or with strain relaxation and surface effects for a freestanding film.

The aim of this work is to study and quantify the effect of FIB during TEM sample fabrication on FeRh phase transition. Additionally, the possibilities of utilizing FIB for FeRh investigations are exploited, such as using ion irradiation for local tuning of the transition temperature.

[1]The name "4D-STEM" refers to recording 2D images of a converged electron probe, over a 2D grid of probe positions. The resulting datasets are 4D, hence the term 4D-STEM, which means all forms of scattering measurements where 2D images of a STEM probe are recorded, either in real or diffraction space, for a 2D grid of probe positions.

4. Experiments

In this chapter, we present the results of our measurements where we investigate the possibilities of phase transition analysis in TEM. These results include the validation of using TEM for FeRh phase transition imaging. Secondly we study the effect of ion irradiation on the phase transition and how it translates to the conventional FIB sample fabrication processes. This chapter includes sample fabrication process description, the impact of used methods on the final samples, temperature dependence of magnetic phase, irradiation damage and ion dose quantification. All instrumental information is mentioned in Supplementary materials Section 5.1.

Thin films grown on a substrate can be studied in TEM in the planar and cross-section view. Here we limit ourselves to one main approach: a freestanding thin film on a TEM grid. We aim to study the effects of Ga ion irradiation using this type of samples, and then use the knowledge gained to evaluate the properties and viability of more commonly used TEM sample types - namely the TEM lamella and a frame mounted on a microelectromechanical system chip (MEMS). In this chapter, we focus only on the freestanding film sample preparation process, with the other two being described in Supplementary materials Section 5.2.

4.1. TEM sample fabrication

A freestanding film is a thin layer without any underlying platform. In case of epitaxially grown films on the substrate, it is necessary to selecively remove the substrate, which leaves a thin electron transparent layer. MgO substrate, that is used for FeRh growth, can be dissolved through chemical etching with an aqueous solution of ethylenediaminetetraacetic acid (EDTA), which dissolves the MgO, but leaves the FeRh layer intact [12, 27].

The fabrication process of such a sample can be seen in schematics in Figure 4.1. First, FeRh is film is grown onto a MgO substrate via Magnetron sputtering (more information in Supplementary materials Section 5.2). Then the sample is submerged into an aqueous solution of EDTA at 80 °C for 12 hours, until the substrate detaches, which leaves the thin FeRh film floating in the solution. The film is then fished out of the EDTA and finally placed onto a TEM grid.

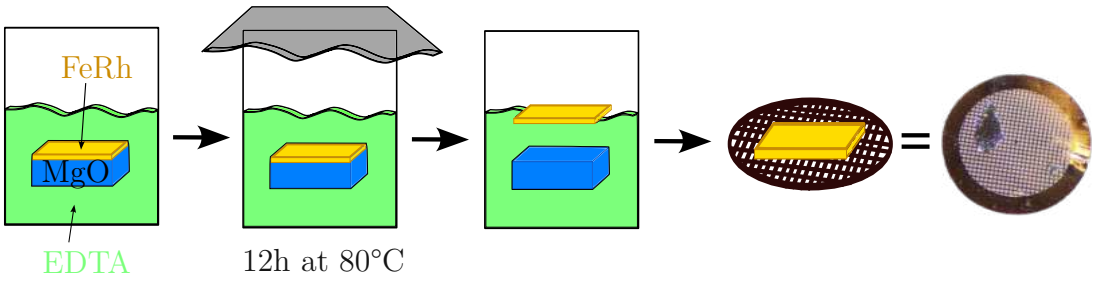

Figure 4.1: A freestanding film fabrication process via Magnetron and chemical etching. First, FeRh is film is grown onto a MgO substrate via Magnetron. Then the sample is submerged into an aqueous solution of EDTA at 80 °C for 12 hours, until the substrate detaches, leaving the thin FeRh film floating atop the surface. The film is the fished out of the EDTA and placed onto a TEM grid.

4.2. Analysis of fabricated samples

Phase transition properties of thin FeRh film were studied using vibrating sample magnetometer (VSM; more details in Section 5.1). We measured the temperature dependence of magnetization, and the result of the measurement can be seen in Figure 4.2. The black hysteresis loop corresponds to FeRh film on MgO substrate. On heating, the transition begins around 390 K and finishes around 420 K, while on cooling it begins around 380 K and finishes around 340 K. There is a small residual magnetization in the AF phase, which changes to around 1000 A/m in the FM phase. The red hysteresis loop corresponds to the freestanding film. We can see that on heating, the phase transition begins around 330 K and ends around 360 K, while on cooling it begins around 320 K and ends near 280 K, making the hysteresis about 50 K wide. We can also see that the film has a residual magnetization of around 500 kA/m in the AF phase, which grows to slightly over 1000 kA/m in the FM phase. The data shows that removing the substrate caused the temperature hysteresis loop to widen and shifted both the onset temperatures to lower values. It also increased the residual magnetization around 5 times compared to FeRh on substrate. However, the transition is preserved, which allows us to study it in TEM. The difference between film on substrate and freestanding film can be explained by relaxation of compressive strain, as discussed in Chapter 2.3.

We then put the sample into TEM and heated it *in-situ* and imaged the film at different temperatures. In Figure 4.3, we can see LTEM images of a part of the film transitioning from the AF phase to the FM phase. Figure (a) corresponds to the film in the viewfield being AF. In Figure (b), we can see the FM spreading from the tom right corner. The black loop-like textures are of topological origin. As discussed in Section 2.1, the crystal lattice of FeRh changes throughout the transition - in FM phase it is larger by around 1%. Therefore, this increase in volume manifests as a bending of the film. When the film bends, different diffraction conditions are met for differently bent parts of the film, and so we see those bent areas as dark. Figure (c) represents the film in the whole viewfield being FM. We can again see the black topological contours here, but there are some thin white lines visible, usually running perpendicular to those black topological contours. These are the domain walls in the FM FeRh. This transition begins at 358 K and ends at 365 K. That corresponds to the latter stage of the transition, when most of the film is already

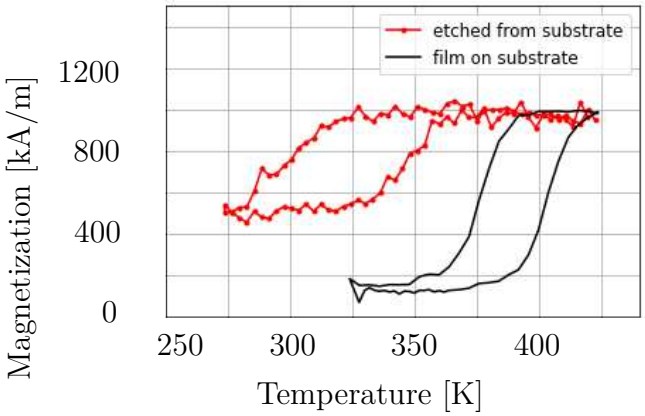

Figure 4.2: VSM measurement of both the freestanding film (red hysteresis loop) and film on substrate (black hysteresis loop).

FM. This area has a locally higher transition temperature, which could be explained by the presence of a crack in the film. A crack may introduce strain to the area, which is hard to quantify, but the effect of it is the stabilization of whatever magnetic phase is present.

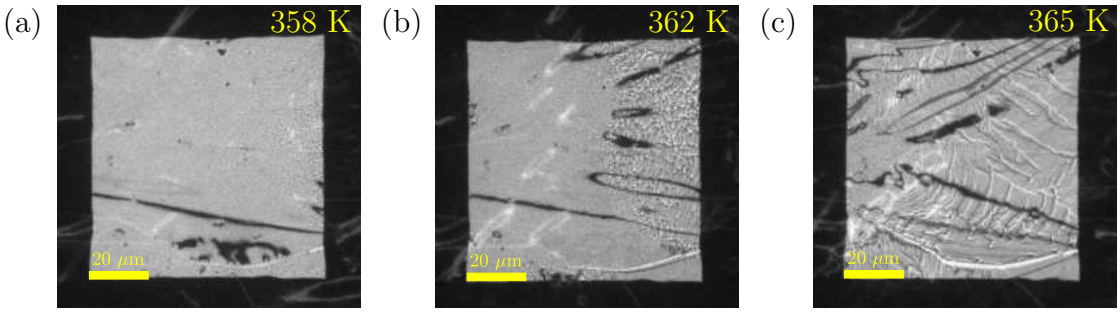

Figure 4.3: The phase transition of freestanding FeRh film on TEM grid from AF to FM phase. (a) Corresponds to the whole film in this area being AF. (b) FM phase starts spreading across the viewfield (the more textured, rough area on the right). (c) The whole film in this viewfield is FM. Black lines correspond to film bending caused by increase in lattice parameter in the FM phase, while white lines correspond to FM domain walls.

4.3. Irradiation

Once we demonstrated reliable way to image the phase transition in FeRh using TEM, we investigated the effects of ion irradiation on the phase transition properties. The irradiation was induced using Dual beam system containing Scanning Electron Microscope and FIB (more information in Supplementary materials Section 5.1. The ion dose D experienced by the specimen using FIB can be quantified as:

$$D = \frac{It_{\mathrm{D}}}{p_{\mathrm{x}}p_{\mathrm{y}}e}N, \tag{4.1}$$

where I stands for the ion current, t_D is the dwell time, e stands for the elemental charge, the parameters p_x and p_y stand for pitch in x and y direction, which represents the distance between adjacent points irradiated for t_D. N stands for the number of passes the ion beam makes over the sample. Detailed description of the irradiation parameters can be found in Supplementary materials Section 5.3.

We then designed a pattern mask to be irradiated with different dose values. This pattern mask is shown in Figure 4.4. It consists of 16 squares, each 6×6 μm^2 in area, and are irradiated with dose values listed in Table 4.1. Various doses were achieved by increasing the number of passes N by a factor of 2 in between the squares, starting at 1 in the first square going up to 2^{15} in the 16th.

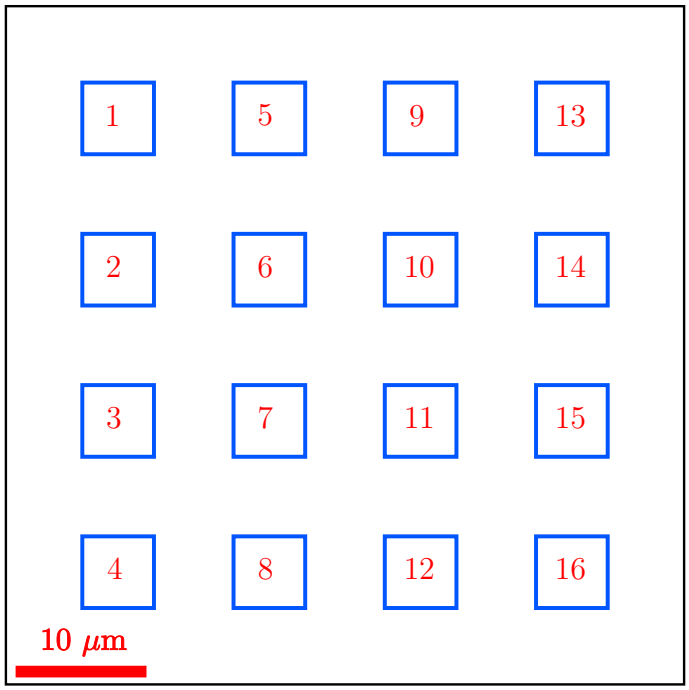

Figure 4.4: Pattern mask for irradiation with FIB.

square number	dose [Ions/cm^2]	square number	dose [Ions/cm^2]
1	$5.94 \cdot 10^9$	9	$1.52 \cdot 10^{12}$
2	$1.19 \cdot 10^{10}$	10	$3.04 \cdot 10^{12}$
3	$2.38 \cdot 10^{10}$	11	$6.08 \cdot 10^{12}$
4	$4.75 \cdot 10^{10}$	12	$1.36 \cdot 10^{13}$
5	$9.5 \cdot 10^{10}$	13	$2.72 \cdot 10^{13}$
6	$1.9 \cdot 10^{11}$	14	$5.44 \cdot 10^{13}$
7	$3.8 \cdot 10^{11}$	15	$1.09 \cdot 10^{14}$
8	$7.6 \cdot 10^{11}$	16	$2.18 \cdot 10^{14}$

Table 4.1: Ion doses for each square in the irradiation mask.

In Figure 4.5 we can see the irradiated film from LTEM overlaid with the pattern mask. This image was taken at 291 K, so it corresponds to AF phase for unirradiated

film. We can see 3 types of texture in the squares. The first one (squares numbers 1-6) is the same as the surrounding film, indicating the AF phase. We can conclude, that the dose received by these areas was low enough to not change the magnetic phase of the irradiated areas. The other type of texture is visible in squares are numbers 7-11. It is different than surrounding film, and is comparable to the FM phase visible in Figure 4.3. We can therefore conclude, that the ion dose received by these areas was high enough to induce the transition into the FM phase. The last type of texture in this figure is visible in squares number 12-16, which experienced the highest doses. This high dose led to the disappearance of magnetic domain walls, indicating the change in magnetic ordering.

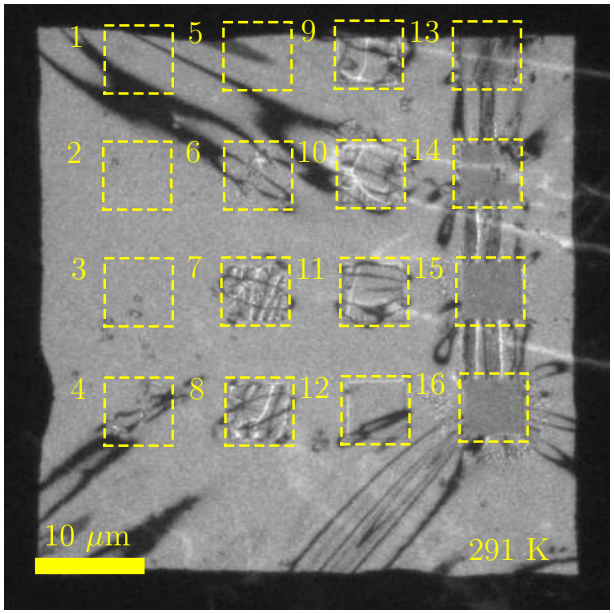

Figure 4.5: The irradiated pattern, image from LTEM, at 291 K. Squares 1-6 are AF, squares 7-11 are FM, squares 12-16 are in neither of those phases.

As magnetic phases in FeRh are connected to the crystalline structure, another way to differentiate between phases is through diffraction patterns. While AF and FM, FeRh has the BCC crystal lattice, in the PM phase it has the FCC lattice. As those two crystalline structures produce different diffraction patterns, we can use the evolution of diffraction patterns to estimate the crystalline structure of the film. In Figure 4.6 we can see the diffraction patterns from areas form the image above. (a) is the diffraction pattern of unirradiated film, while (b) represents area 8, (c) represents area 11 and (d) represents area 16. In the diffraction patterns, green dashed lines represent the 100 and 010 axes and diffraction spots (100), (010) and (110) are circled. Comparing the images, we can see the disappearance of the (100) and (010) spots, which indicates the disappearance of the BCC phase. The (110) and (200) spots seemingly remain, but that is not true, as the FCC crystal lattice has one of its diffraction spots in almost the same space. We can therefore conclude, that these areas received so high a dose that it made them PM. This agrees well with the measurements of Aikoh and colleagues, who too experienced the disappearance of the (100) peaks, while the (200) peak remained strong [1]. Another good agreement with their work is that the (100) and (010) peaks disappear with the dose crossing the 10^{13} threshold. We can also see the introduction of more defects by the ion

beam with increasing dose from the blurring and lengthening of the diffraction spots.

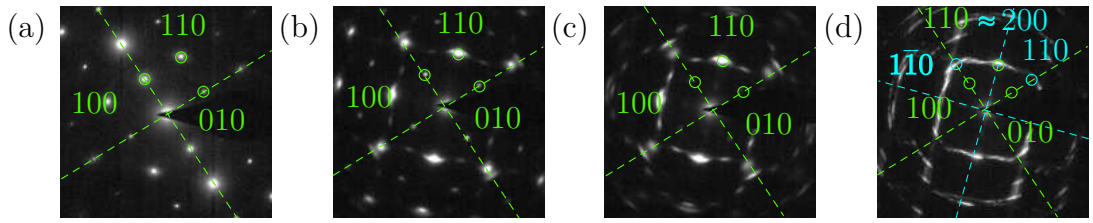

Figure 4.6: Diffraction patterns from (a) unirradiated film and from irradiated areas (b) 8, (c) 11 and (d) 16.

In figure 4.7, a summary of the irradiation experiments is presented. On the x-axis is the ion dose and above that is the magnetic phase the dose corresponds to, LTEM image of the irradiated area, the crystalline structure and a diffraction pattern from the irradiated area.

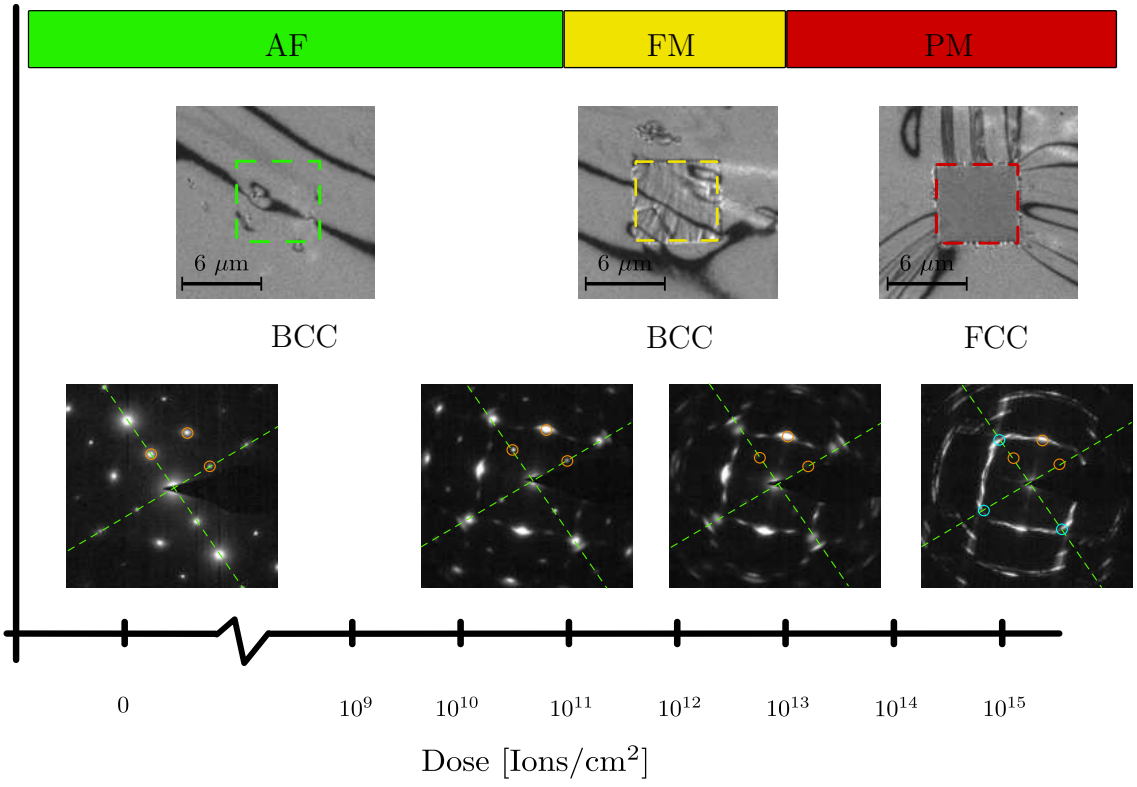

Figure 4.7: Ion doses and their corresponding magnetic phase, crystalline structure, irradiated area in LTEM and diffraction pattern.

In order to investigate the exact properties of phase transition, we can evaluate the transition temperature as the function of dose. When the material changes from AF to FM at room temperature, the dose effectively loweres the transition temperature under room temperature. From temperature dependent LTEM on FeRh irradiated by certain dose, we can extract the transition temperature for that dose as shown in Figure 4.8.

Blue points represent cooling, red points represent heating. We can see that the transition temperature decreases with increasing ion dose. This temperature shift was measured only for the lower doses, so even the area with the highest dose in the graph is FM at room temperature. We have to be mindful of approximating the transition temperature of the whole film by the "middle point" in the temperature hysteresis, which might change the real transition temperature in certain regions of the film even by 20 K, and also that there might be an inhomogeneous distribution of temperature across the sample.

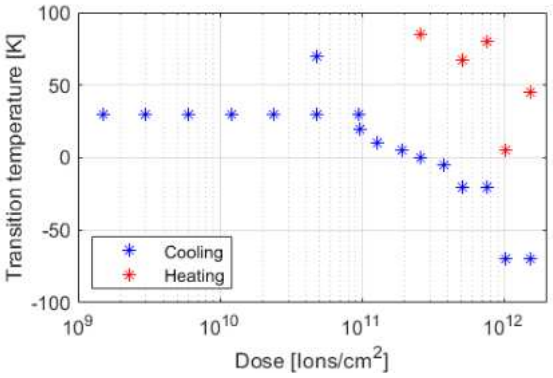

Figure 4.8: Transition temperature on both heating and cooling for lower doses.

From all this data, we can conclude that ion doses lower than 10^{11} ions/cm^2 do not change the material significantly, only slightly lowering the transition temperature by a few tens of K. Doses between 10^{11} and 10^{13} ions/cm^2 make FeRh transition into the FM state, effectively lowering the transition temperature by more than 80 K and doses higher than 10^{13} ions/cm^2 change the material even more, making it PM, which would correspond with decrease in temperature of over 300 K.

4.4. TEM sample analysis

Knowing the effect of irradiation on thin FeRh film, we wanted to evaluate the effect of irradiation in conventionally used TEM sample geometries prepared by FIB, namely a cross-section lamella and a freestanding window mounted on a MEMS chip. The window (frame) is a piece of freestanding film, that has a carbon frame deposited around the edge to maintain its mechanical stability, before being attached to a MEMS chip. TEM lamella is a cross-section sample of a thin film on a substrate, polished to electron transparency using FIB. The fabrication process of both is described in detail in Supplementary materials Section 5.2. All of the fabrication steps after film preparation were done using FIB, therefore the samples experienced considerable amount of ion irradiation during fabrication, and we wanted to estimate its effect on phase transition. As the interpretation of magnetic imaging using LTEM was not conclusive, we recorded the diffracion patterns from those samples to estimate the structural properties of the specimens.

In Figure 4.9(a), we can see the TEM lamella and a closeup on area of interest. A 180 nm film of FeRh was deposited on MgO(001) substrate and covered by a carbon cap,

then it was cut out from the sample and placed on a MEMS chip, where it was thinned to electron transparency. The disc superimposed over the lamella denotes the area, from which the diffraction pattern was taken. It should be noted, that both a part of the carbon cap and a part of the MgO substrate are included in the diffraction pattern from this area. In section (b) we can see the diffraction pattern of pure MgO(001) substrate with crystallographic orientation $(1\bar{1}1)$ and $(\bar{1}11)$ denoted by the dashed lines. In section (c) we can see the diffraction pattern from the FeRh part of the lamella. The orange dashed lines correspond to the same crystallographic orientations $(1\bar{1}1)$ and $(\bar{1}11)$ of MgO as in Figure (b), while blue dashed lines correspond to crystallographic orientations (110) and $(1\bar{1}0)$ of FeRh. There are many diffraction points with many different origins in the image, some of the indetifiable being marked in circles. The orange circled spots correspond with those from the MgO diffraction pattern, we can therefore say those come from the MgO substrate. The blue circled spots on lines correspond to FCC FeRh in the (001) orientation, which is the orientation in which FeRh grew on the substrate. The weakly visible red circled spots in the middle of the pattern correspond to BCC FeRh (001). There are many other diffraction spots, some of which can be the result of distorted FeRh lattice in the contact region with the substrate, some other may be caused by the part of the capping layer, that is directly in contact with FeRh and therefore may be crystallic. The exact origin of those spots is unclear, but they do not prevent a conclusion to be made. From the presence of both the FCC and BCC-characteristic spots and from the lack of measurable phase transition, we can conclude that the lamella has been irradiated so heavily that it is just between the FM and the PM state.

The second studied sample geometry, frame mounted on a MEMS chip, can be seen in Figure 4.10(a), with a closeup on a electron-transparent part of the chip, covered only by the FeRh film. Section (b) shows the diffraction pattern of unirradiated thin FeRh film, with the 010 and 100 crystallographic orientations denoted by the dashed lines. Section (c) presents the diffraction pattern form the closeup area. The dashed lines again denote the main crystallographic orientations, spot (110) is marked, as are the spaces where diffraction spots (100) and (010) should be. The lack of measurable transition and the missing diffraction spots again suggests the material to be so heavily irradiated that it became PM.

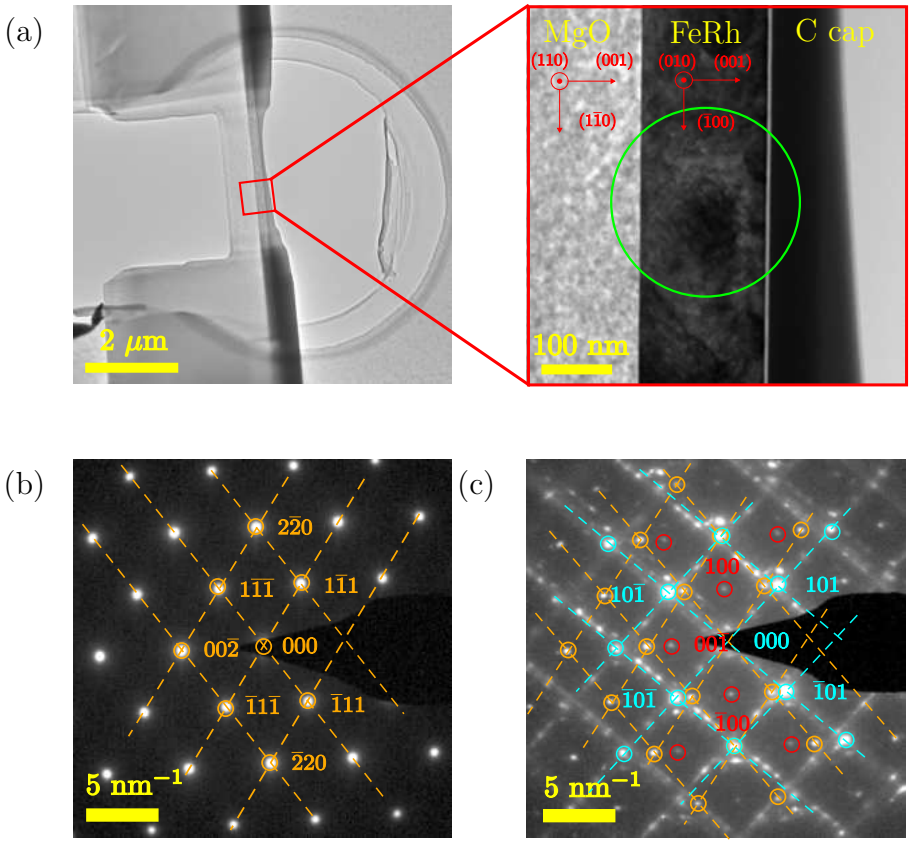

Figure 4.9: (a) Closeup of a thinned part of a TEM lamella, with a cutout depicting the region of interest, appended with the crystallographic orientation of different layers and a disc denoting the area from which the diffraction pattern was taken. (b) Diffraction pattern of the pure MgO(001) substrate. (c) Diffraction pattern from the part of the TEM lamella marked by the disc.

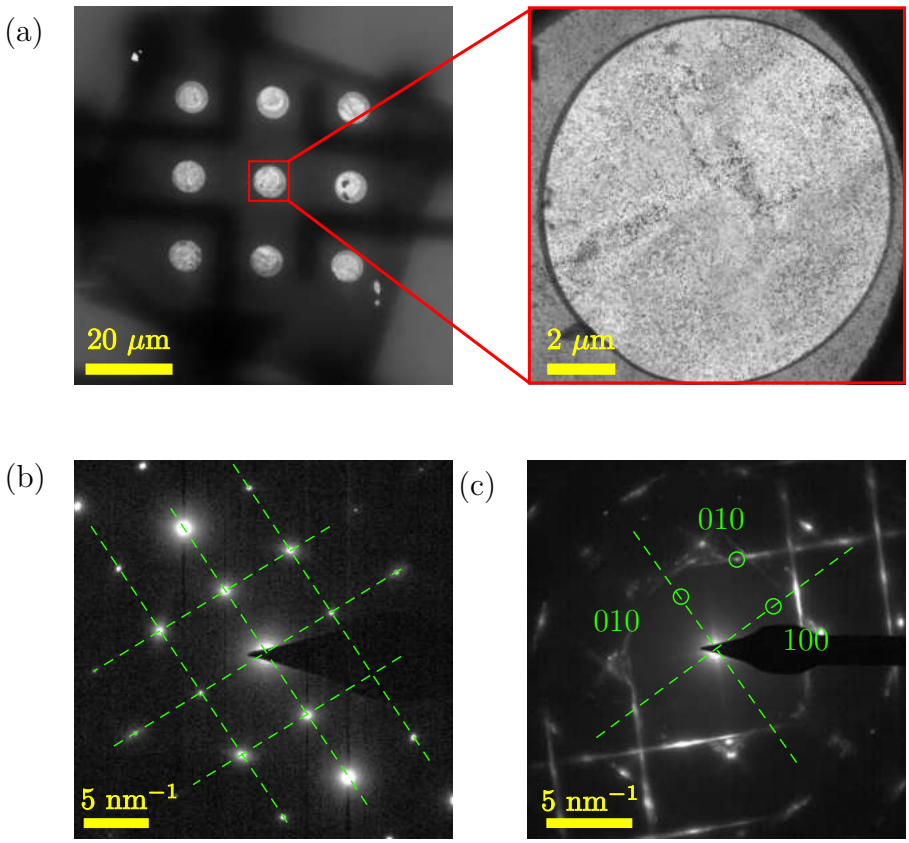

Figure 4.10: (a) Framed film mounted on a MEMS chip and a closeup on an electron transparent part of the chip covered only by the thin FeRh film. (b) Diffraction pattern of unirradiated FeRh thin film. (c) Diffraction pattern from the closeup region.

4.5. Consequences of using FIB for sample preparation

The data we collected suggests that FIB is a very invasive technique and using it for sample preparations results in the sample being changed from its original state. The ion irradiation induces a lot of defects so that the sample is no longer representative of the original system it was taken from. Our measurements on FeRh show that our samples are heavily irradiated, therefore the phase transition in them is shifted to much lower temperatures. The dose is so high, that the sample is just in the middle of transitioning from the FM to the PM state, if not entirely PM.

4.6. Benefits of irradiation for use in FeRh study

Using FIB for sample fabrication changes the sample from its original state, therefore it is not an ideal technique for sample fabrication. It can, however, serve another purpose. As we showed in Section 4.3, ion irradiation lowers the transition temperature. Therefore, controlled ion irradiation can be potentially used to locally tune the transition temperature in range of tens of K for lower doses (around 10^{10}) or even in hundreds of K for higher doses.

Conclusion

The aim of this thesis was to image the magnetostructural phase transition in metamagnetic FeRh system using TEM. As the TEM specimen are often prepared using FIB, the influence of ion irradiation on FeRh phase transition was investigated with respect to the phase transition properties of the original thin film form of FeRh.

The theoretical part of the thesis covers basics of nanomagnetism, where we explored the origin of magnetism in solids, analyzed the structure of different types of magnetic ordering found in solids and described the interactions of different magnetic orderings with magnetic field. We also described the phase transitions between those magnetic orderings. We then talked about the phase transition of FeRh and its tunability, specifically about the thin film variant of FeRh. We continued with a short insight into the topic of TEM, the construction of the microscope itself and some usual imaging modes with special attention to magnetic imaging techniques. A recherche of the state of the art in magnetic imaging of FeRh was also presented.

In the experimental part, we described the fabrication processes of FeRh thin film samples for TEM and their subsequent post-fabrication analysis. The substrate was removed from under a thin film to achieve electron transparency, and we studied the effects removing the substrate has on the phase transition of FeRh. We then heated the sample *in-situ* and imaged the phase transition in TEM. We then analyzed how ion irradiation applied by FIB influences the phase transition and measured the changes induced in FeRh thin film for multiple different ion doses. We found that ion irradiation in small amounts (in order of 10^{10} ions per cm^2) lowers the transition temperature in order of tens of K, while higher doses (up to 10^{13} ions per cm^2) make FeRh transition into its FM phase. Ion doses of even higher magnitude change the material further, making it undergo its second phase transition to the PM phase.

We then fabricated a classical TEM lamella and framed window mounted on a MEMS chip and analyzed their phase transition properties. The lack of any detectable phase transition, coupled with structural analysis of the samples revealed that the fabrication process using FIB is inherently destructive. During the fabrication process, the samples received doses high enough to make them transition to the PM phase. We therefore concluded that the fabrication of TEM samples using FIB changes the structure of the material from its original state. Another important conclusion is that we can potentially use ion irradiation to locally influence the transition temperature of FeRh, making ion irradiation very useful tool for the design of special temperature-dependent structures.

Further research will be aimed at studying the effect of post-fabrication annealing and the possibility of restoring the crystalline structure of FIB-made samples, improvement of sample fabrication procedures using FIB to minimize irradiation, as well as further exploring the localized tunability of transition temperature in FeRh.

Literature

[1] AIKOH, K.; KOSUGI, S.; MATSUI, T.; IWASE, A. Quantitative control of magnetic ordering in FeRh thin films using 30 keV Ga ion irradiation from a focused ion beam system. *Journal of Applied Physics*. 2011, vol. 109, no. 7. ISSN 0021-8979. Available from DOI: 10.1063/1.3549440.

[2] ALMEIDA, Trevor P.; MCGROUTHER, Damien; TEMPLE, Rowan; MASSEY, Jamie; LI, Yue, et al. Direct visualization of the magnetostructural phase transition in nanoscale FeRh thin films using differential phase contrast imaging. *Physical Review Materials*. 2020, vol. 4, no. 3, pp. 1–12. ISSN 24759953. Available from DOI: 10.1103/PhysRevMaterials.4.034410.

[3] ALMEIDA, Trevor P.; TEMPLE, Rowan; MASSEY, Jamie; FALLON, Kayla; MCGROUTHER, Damien, et al. Quantitative TEM imaging of the magnetostructural and phase transitions in FeRh thin film systems. *Scientific Reports*. 2017, vol. 7, no. 1, pp. 1–11. ISSN 20452322. Available from DOI: 10.1038/s41598-017-18194-0.

[4] ARREGI, Jon Ander; CAHA, Ondřej; UHLÍŘ, Vojtěch. Evolution of strain across the magnetostructural phase transition in epitaxial FeRh films on different substrates. *Physical Review B*. 2020, vol. 101, no. 17, p. 174413. ISSN 2469-9950. Available from DOI: 10.1103/PhysRevB.101.174413.

[5] BALDASSERONI, C.; BORDEL, C.; GRAY, A. X.; KAISER, A. M.; KRONAST, F., et al. Temperature-driven nucleation of ferromagnetic domains in FeRh thin films. *Applied Physics Letters*. 2012, vol. 100, no. 26. ISSN 00036951. Available from DOI: 10.1063/1.4730957.

[6] BARANOV, N V; BARABANOVA, E A. *Electrical resistivity and magnetic phase transitions in modified FeRh compounds*. 1995. Tech. rep. Journal of Alloys and Compounds 219.

[7] BARUA, Radhika; JIMÉNEZ-VILLACORTA, Félix; LEWIS, L. H. Towards tailoring the magnetocaloric response in FeRh-based ternary compounds. *Journal of Applied Physics*. 2014, vol. 115, no. 17. ISSN 00218979. Available from DOI: 10.1063/1.4854975.

[8] BENNETT, S. P.; HERKLOTZ, A.; CRESS, C. D.; IEVLEV, A.; ROULEAU, C. M., et al. Magnetic order multilayering in FeRh thin films by He-Ion irradiation. *Materials Research Letters*. 2018, vol. 6, no. 1, pp. 106–112. ISSN 21663831. Available from DOI: 10.1080/21663831.2017.1402098.

[9] BLUNDELL, S. *Oxford Master Series in Condensed Physics*. 2001. Tech. rep.

[10] CEBALLOS, A.; CHEN, Zhanghui; SCHNEIDER, O.; BORDEL, C.; WANG, Lin Wang, et al. Effect of strain and thickness on the transition temperature of epitaxial FeRh thin-films. *Applied Physics Letters*. 2017, vol. 111, no. 17. ISSN 00036951. Available from DOI: 10.1063/1.4997901.

[11] COEY, J. M. D. *Magnetism and Magnetic Materials*. Cambridge University Press, 2001. ISBN 9780521016766. Available from DOI: 10.1017/CBO9780511845000.

[12] EDLER, Tobias; MAYR, Stefan G. Film lift-off from MgO: Freestanding single crystalline Fe-Pd films suitable for magnetic shape memory actuation - And beyond. *Advanced Materials*. 2010, vol. 22, no. 44, pp. 4969–4972. ISSN 09359648. Available from DOI: 10.1002/adma.201002183.

[13] FALLOT, M.; HOCART, R. Sur l'apparition du ferromagnétisme par élévation de température dans des alliages de fer et de rhodium. *Revue Scientifique*. 1939, vol. 77, pp. 498–499.

[14] FENG, Zexin; YAN, Han; LIU, Zhiqi. *Advanced Electronic Materials*. Vol. 5, Electric-Field Control of Magnetic Order: From FeRh to Topological Antiferromagnetic Spintronics. Blackwell Publishing Ltd, 2019. No. 1. ISSN 2199160X. Available from DOI: 10.1002/aelm.201800466.

[15] FINA, Ignasi; DIX, Nico; MENÉNDEZ, Enric; CRESPI, Anna; FOERSTER, Michael, et al. Flexible Antiferromagnetic FeRh Tapes as Memory Elements. *ACS Applied Materials and Interfaces*. 2020, vol. 12, no. 13, pp. 15389–15395. ISSN 19448252. Available from DOI: 10.1021/acsami.0c00704.

[16] FRANCO, V.; BLÁZQUEZ, J. S.; INGALE, B.; CONDE, A. *Annual Review of Materials Research*. Vol. 42, The magnetocaloric effect and magnetic refrigeration near room temperature: Materials and models. 2012. ISSN 15317331. Available from DOI: 10.1146/annurev-matsci-062910-100356.

[17] GATEL, C.; WAROT-FONROSE, B.; BIZIERE, N.; RODRÍGUEZ, L. A.; REYES, D., et al. Inhomogeneous spatial distribution of the magnetic transition in an iron-rhodium thin film. *Nature Communications*. 2017, vol. 8, pp. 1–8. ISSN 20411723. Available from DOI: 10.1038/ncomms15703.

[18] HEIDARIAN, A.; BALI, R.; GRENZER, J.; WILHELM, R. A.; HELLER, R., et al. Tuning the antiferromagnetic to ferromagnetic phase transition in FeRh thin films by means of low-energy/low fluence ion irradiation. *Nuclear Instruments and Methods in Physics Research, Section B: Beam Interactions with Materials and Atoms*. 2015, vol. 358, pp. 251–254. ISSN 0168583X. Available from DOI: 10.1016/j.nimb.2015.06.027.

[19] HIROHATA, Atsufumi; YAMADA, Keisuke; NAKATANI, Yoshinobu; PREJBEANU, Lucian; DIÉNY, Bernard, et al. *Journal of Magnetism and Magnetic Materials*. Vol. 509, Review on spintronics: Principles and device applications. Elsevier B.V., 2020. ISSN 03048853. Available from DOI: 10.1016/j.jmmm.2020.166711.

[20] JUNGWIRTH, T.; MARTI, X.; WADLEY, P.; WUNDERLICH, J. Antiferromagnetic spintronics. *Nature Nanotechnology*. 2016, vol. 11, no. 3, pp. 231–241. ISSN 1748-3387. Available from DOI: 10.1038/nnano.2016.18.

[21] KOUVEL, J. S. Unusual Nature of the Abrupt Magnetic Transition in FeRh and Its Pseudobinary Variants. *Journal of Applied Physics*. 1966, vol. 37, no. 3, pp. 1257–1258. ISSN 0021-8979. Available from DOI: 10.1063/1.1708424.

[22] KOUVEL, J. S.; HARTELIUS, C. C. Anomalous magnetic moments and transformations in the ordered alloy FeRh. *Journal of Applied Physics*. 1962, vol. 33, no. 3, pp. 1343–1344. ISSN 00218979. Available from DOI: 10.1063/1.1728721.

[23] LEWIS, L. H.; MARROWS, C. H.; LANGRIDGE, S. Coupled magnetic, structural, and electronic phase transitions in FeRh. *Journal of Physics D: Applied Physics*. 2016, vol. 49, no. 32, p. 323002. ISSN 13616463. Available from DOI: 10.1088/0022-3727/49/32/323002.

[24] LOMMEL, J. M. Magnetic and electrical properties of FeRh thin films. *Journal of Applied Physics*. 1966, vol. 37, no. 3, pp. 1483–1484. ISSN 00218979. Available from DOI: 10.1063/1.1708527.

[25] MAAT, S.; THIELE, J.-U.; FULLERTON, Eric E. Temperature and field hysteresis of the antiferromagnetic-to-ferromagnetic phase transition in epitaxial FeRh films. *Physical Review B*. 2005, vol. 72, no. 21, p. 214432. ISSN 1098-0121. Available from DOI: 10.1103/PhysRevB.72.214432.

[26] MCKINNON, J B; MELVILLE, D; LEE, E W. *The antiferromagnetic-ferromagnetic transition in iron-rhodium alloys*. 1970. Tech. rep. Journal of Physics C: Solid State Physics 3 S46.

[27] MOTYČKOVÁ, K. *Motyčková - MT*. 2020. Tech. rep.

[28] OHTANI, Y.; HATAKEYAMA, I. Antiferro-ferromagnetic transition and microstructural properties in a sputter deposited FeRh thin film system. *Journal of Applied Physics*. 1993, vol. 74, no. 5, pp. 3328–3332. ISSN 00218979. Available from DOI: 10.1063/1.354557.

[29] OHTANI, Y.; HATAKEYAMA, I. Features of broad magnetic transition in FeRh thin film. *Journal of Magnetism and Magnetic Materials*. 1994, vol. 131, no. 3, pp. 339–344. ISSN 03048853. Available from DOI: 10.1016/0304-8853(94)90278-X.

[30] PAPON, P. *The Physics of Phase Transitions*. 2006. Tech. rep. Springer Berlin Heidelberg New York.

[31] PLUMEL, M. L.; ELK, J. van; WELLER, D. *The Physics of Ultra-High-Density Magnetic Recording*. 2001. Tech. rep. (Springer series in surface sciences, ISSN 0931-5195 ; 41. Available also from: http://www.springer.de/phys/.

[32] ROY, S. B.; CHADDAH, P. Experimental study of disorder -influenced first-order transitions in vortex matter and in magnetic systems. *Phase Transitions*. 2004, vol. 77, no. 8-10, pp. 767–790. ISSN 01411594. Available from DOI: 10.1080/01411590410001690891.

[33] ROY, Sindhunil Barman. *Journal of Physics Condensed Matter*. Vol. 25, First order magneto-structural phase transition and associated multi-functional properties in magnetic solids. 2013. No. 18. ISSN 09538984. Available from DOI: 10.1088/0953-8984/25/18/183201.

[34] SHIRANE, G.; CHEN, C. W.; FLINN, P. A.; NATHANS, R. Hyperfine fields and magnetic moments in the FeRh system. *Journal of Applied Physics*. 1963, vol. 34, no. 4, pp. 1044–1045. ISSN 00218979. Available from DOI: 10.1063/1.1729362.

[35] SONG, Sehwan; CHO, Chang woo; KIM, Jiwoong; LEE, Jisung; LEE, Dooyong, et al. Correlation between phase transition characteristics and hydrogen irradiation-induced Frenkel defect formations in FeRh films. *Journal of Alloys and Compounds*. 2022, vol. 901. ISSN 09258388. Available from DOI: 10.1016/j.jallcom.2022.163611.

[36] SUN, Litao; XU, Tao; ZHANG, Ze. *In-Situ Transmission Electron Microscopy*. In-Situ Transmission Electron Microscopy. Springer Singapore, 2023. ISBN 9789811968457. Available from DOI: 10.1007/978-981-19-6845-7.

[37] SUZUKI, Ippei; KOIKE, Takayoshi; ITOH, Mitsuru; TANIYAMA, Tomoyasu; SATO, Tetsuya. Stability of ferromagnetic state of epitaxially grown ordered FeRh thin films. *Journal of Applied Physics*. 2009, vol. 105, no. 7. ISSN 00218979. Available from DOI: 10.1063/1.3054386.

[38] SWARTZENDRUBER, L. J. The Fe—Rh (Iron-Rhodium) system. *Bulletin of Alloy Phase Diagrams*. 1984, vol. 5, no. 5, pp. 456–462. ISSN 0197-0216. Available from DOI: 10.1007/BF02872896.

[39] THIELE, Jan Ulrich; MAAT, Stefan; FULLERTON, Eric E. FeRH/FePt exchange spring films for thermally assisted magnetic recording media. *Applied Physics Letters*. 2003, vol. 82, no. 17, pp. 2859–2861. ISSN 00036951. Available from DOI: 10.1063/1.1571232.

[40] WALTER, Paul H.L. Exchange inversion in ternary modifications of iron rhodium. *Journal of Applied Physics*. 1964, vol. 35, no. 3, pp. 938–939. ISSN 00218979. Available from DOI: 10.1063/1.1713547.

[41] WAYNE, R. C. Pressure Dependence of the Magnetic Transitions in Fe-Rh Alloys. *Physical Review*. 1968, vol. 170, no. 2, pp. 523–527. ISSN 0031-899X. Available from DOI: 10.1103/PhysRev.170.523.

[42] WILLIAMS, David B.; CARTER, C. Barry. *Transmission Electron Microscopy*. Boston, MA : Springer US, 2009. ISBN 978-0-387-76500-6. Available from DOI: 10.1007/978-0-387-76501-3.

[43] YOKOYAMA A', Y; USUKURA, M; YUASA, S; SUZUKI, Y; MIYAJIMA, H, et al. *Journal of-*
." magnetism and magnetic ELSEVIER
materials MFM observation of magnetic phase transitions in ordered FeRh systems. 1998. Tech. rep. ISBN 03048853/98.

[44] ZAKHAROV, A. I.; KADOMTSEVA, A. M.; LEVITIN, R.; PONYATOVSKIĬ, E. G. Magnetic and magnetoelastic properties of a metamagnetic iron-rhodium alloy. *Soviet Physics JETP*. 1964, vol. 19, no. 6, p. 1348. Available also from: http://www.jetp.ras.ru/cgi-bin/dn/e_019_06_1348.pdf.

[45] ZHOU, Xianzhong; MATTHES, Frank; BÜRGLER, Daniel E.; SCHNEIDER, Claus M. Magnetic surface domain imaging of uncapped epitaxial FeRh(001) thin films across the temperature-induced metamagnetic transition. *AIP Advances*. 2016, vol. 6, no. 1. ISSN 21583226. Available from DOI: 10.1063/1.4940758.

List of Abbreviations

AF	Antiferromagnetism, antiferromagnetic
BCC	Body centred cubic crystal lattice
BFP	Back focal plane
CBED	Convergent beam electron diffraction
CTEM	Conventional transmission electron microscopy
DPC	Differential phase contrast
EDTA	Ethylenediaminetetraacetic acid
ETO	Electrical transport option
FCC	Face centred cubic crystal lattice
FIB	Focused ion beam
FM	Ferromagnetism, ferromagnetic
GIS	Gas injection system
HAMR	Heat-assisted magnetic recording
KTO	$KTaO_3$
LTEM	Lorentz transmission electron microscopy
MEMS	Microelectromechanical system
MFM	Magnetic force microscopy
MOKE	Magneto-optical Kerr effect
PM	Paramegnetism, paramagnetic
SAD	Selected area diffraction
SAED	Selected area electron diffraction
SEMPA	Scanning electron microscopy with polarization analysis
STEM	Scanning transmission electron microscopy
STO	$SrTiO_3$
TEM	Transmission electron microscopy, transmission electron microscope
VSM	Vibrating sample magnetometry, vibrating sample magnetometer
XMCD	X-ray magnetic circular dichroism

Supplementary materials

Experimental methodology and parameters

TEM analysis was performed using a FEI Titan Themis 60-300 cubed TEM microscope (TITAN) at the CEITEC Nano facility in Brno. The TITAN possesses a high brightness Schottky field emitter gun with a monochromator and can accelerate the electron beam with voltages ranging from 60 kV up to 300 kV. The beam is then shaped and regulated by a 3-lens condenser system. The TITAN is equipped with a spherical aberration CEOS GmbH corrector. The detection system consists of a fluorescent screen, 4k×4k 16 bit CMOS-based CETA 16M camera with an optic-coupled scintillator, and a set of STEM detectors including a bright field, two dark field, and a high angle annual dark field semiconductor-based detectors and a Lorentz lens, which enables imaging of magnetic structures. The TEM experiments were performed by Ing. Jan Hajduček, and the data processing was done by the author.

All **VSM magnetic measurements** were carried out in Cryogenic-free VSM and ETO measurement system by Versalab. It is a vibrating sample magnetometer (VSM) with an electrical transport option (ETO), capable of applying magnetic field up to 3 T within a temperature range from 50 K up to 400 K, which can be extended up to 1000 K by an oven kit. The VersaLab VSM consists primarily of a linear motor for vibrating the sample and a pickup coil set for detection. With its operation frequency of 40 Hz and a relatively large oscillation amplitude of a few mm, the system is capable of resolving magnetization changes of less than 1 µemu with 1 s data averaging. The VSM system disposes with two sets of coils (standard and large) for different sample sizes. For our samples on TEM grids, the standard pickup coilset was used.

FIB experiments, consisting of lamella and framed window preparation and irradiation experiments, were carried out mostly using a dual-beam Focused Ion Beam/Scanning Electron Microscope FEI Helios NanoLab 660 (HELIOS), with some irradiation experiments done using Focused Ion Beam/Scanning Electron Microscope TESCAN LYRA3 (LYRA). Both of these systems possess a Schottky field emitter gun, HELIOS with a monochromator, and a Ga liquid metal ion source, which operates up to 30 kV. Both also allow for precise irradiation experiments and fairly good ion dose quantification with a wide range of adjustable parameters for FIB. For HELIOS, a 3D-movable and rotatable sample stage, a nanomanipulator and a gas injection system (GIS) with two elements (W and C) make this system ideal for preparation of samples such as the TEM lamella or frame. Experiments performed in LYRA were performed by Ing. Jan Hajduček.

***In-situ* heating** of the samples to induce the phase transition was done using Gatan cryoholder and a Protochips Fusion select Electrothermal MEMS chip.

The cryoholder can hold the classical 3 mm TEM grids, therefore it was used for experiments with freestanding film on grid. It can heat the sample up to 90 °C and provides cooling under -170 °C. With such a wide range of accessible temperatures, it is perfectly suited to map the transition temperatures of slightly irradiated samples, that undergo the

phase transition in temperatures just under 0 °C.

Figure 5.1: Gatan single tilt liquid nitrogen cryo transfer holder. Adapted from this webpage.

The Protochips Fusion select Electrothermal MEMS chip was used for heating both the lamella and the framed window. It provides heating up to 1200 °C, but has no cooling function. It can therefore be used only for heating experiments, but can potentially provide a way to induce even the second phase transition from FM to PM phase without any irradiation. The loading of samples onto the MEMS chip is, however, accessible only through attaching by ion deposition, which inherently exposes the sample to ion irradiation.

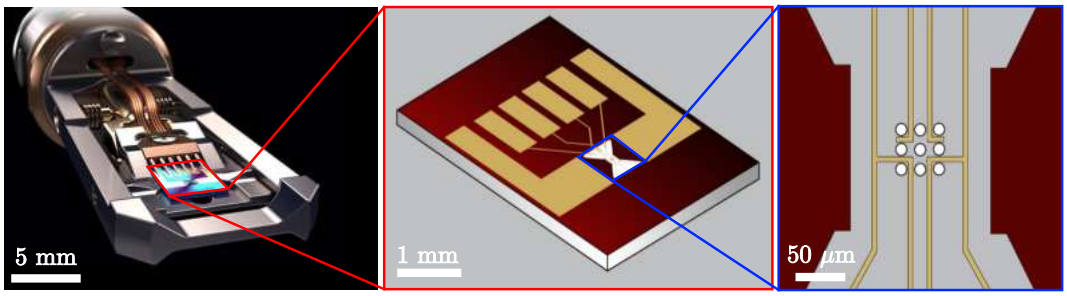

Figure 5.2: Protochips Fusion select Electrothermal MEMS chip. Adapted from the Protochips website.

Epitaxial FeRh films were grown onto a single-crystal MgO(001) substrate using Magnetotron sputtering from an equiatomic FeRh target. The substrates were loaded into the vacuum chamber and preheated for 1 hour at 650 K. The FeRh was grown at the same temperature under Ar gas pressure of 2,7 $\times 10^{-3}$ mbar using a sputter power of 50 W,

which resulted in a deposition rate of about 2 nm/min. The films were annealed afterwards at 1000 K for 45 minutes to obtain the desired CsCl-type crystallographic structure and to improve their chemical ordering. The film growth was performed by M.Sc. Jon Ander Arregi, Ph. D.

TEM sample fabrication

One of the main properties of a TEM sample is being transparent for highly accelerated electrons. This means being very thin (around 50 nm or even less, depending on the material), which can be achieved in multiple ways. The geometry of a TEM sample is limited by the dimensions of used TEM sample holder, which usually permits samples of only a few mm in diameter (most TEM holders can accommodate samples up to 3 mm in diameter).

A **TEM lamella** is basically a thin plate of material, cut out of the sample perpendicularly to its surface. This "cutting" is achieved via FIB, with the whole fabrication process represented on Figures 5.3 (a)-(f). The whole process begins by depositing a protective capping layer via the *gas injection system* (GIS) to minimize damage to the region of the layer we actually want to study. We then cut out a plate approximately 1 μm thic, lift it out with a nanomanipulator and attach it to a Cu TEM grid via GIS, which is shown in Figure 5.3 (h). There are two possible ways to attach the lamella to the TEM grid, which are shown in Figure 5.3 (g). The last step in the fabrication process consists of polishing the lamella with FIB to make it electron transparent, which corresponds to thickness under 100 nm. In this step, it is especially important to be careful, as if the protective capping layer is destroyed, the studied layer follows it in short order and the whole sample becomes unusable.
Lamella is a often used type of sample for TEM measurements because of the relative ease and speed with which it can be manufactured, as well as the relatively broad dual-beam FIB/SEM system availability.

Framed window mounted on a MEMS chip is also a thin plate of the studied material, but in contrast to a lamella (which is a cross-section-type sample), in this case the plate is cut from a freestanding film, so it is a planar-type sample. The fabrication process of a chip-mounted frame sample is represented on Figures 5.4 (a)-(f). The process begins by depositing a protective cap via GIS to minimize the ion damage to the thin layer itself. It continues with depositing a "frame" on top of the cap - a square with sides few μm thick. This frame acts as a support, that mechanically holds the whole structure together. It is then cut out and lifted out and placed over a MEMS chip, which can be seen in Figure 5.4 (g). There it is attached via GIS to the electrical contacts facilitating heating, shown of Figure 5.4 (e) and (f).

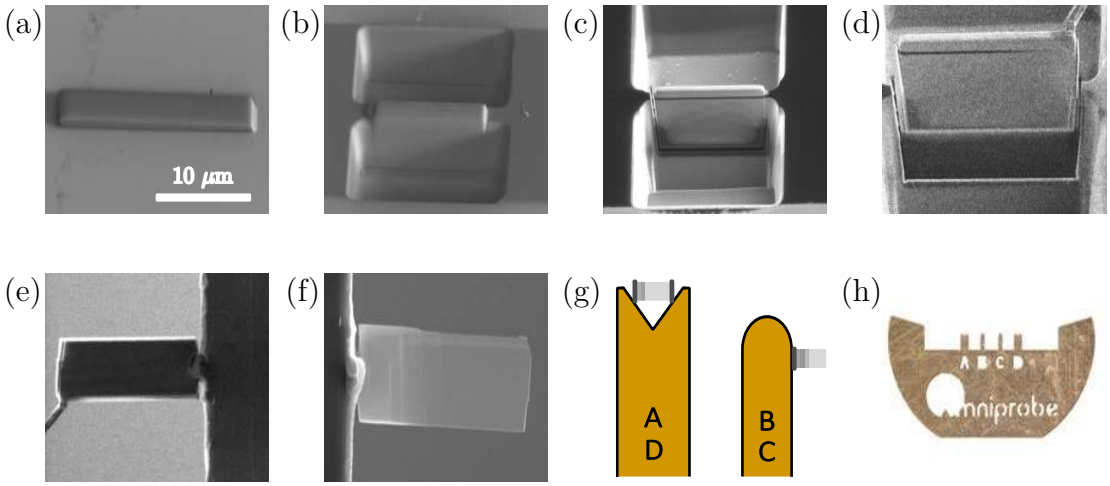

Figure 5.3: Fabrication process of a TEM lamella via FIB. (a) Deposition of a capping layer on top of the thin film via GIS, followed by milling shown in (b) and (c). (d) Lift-off of the unpolished lamella with nanomanipulator and (e) its subsequent attachment to the TEM grid, followed by (f) polishing it to electron transparency. (g) Two ways of attaching the lamella the the TEM grid. Letters correspond to mounting positions of the TEM grid, shown in (h). Adapted from this website.

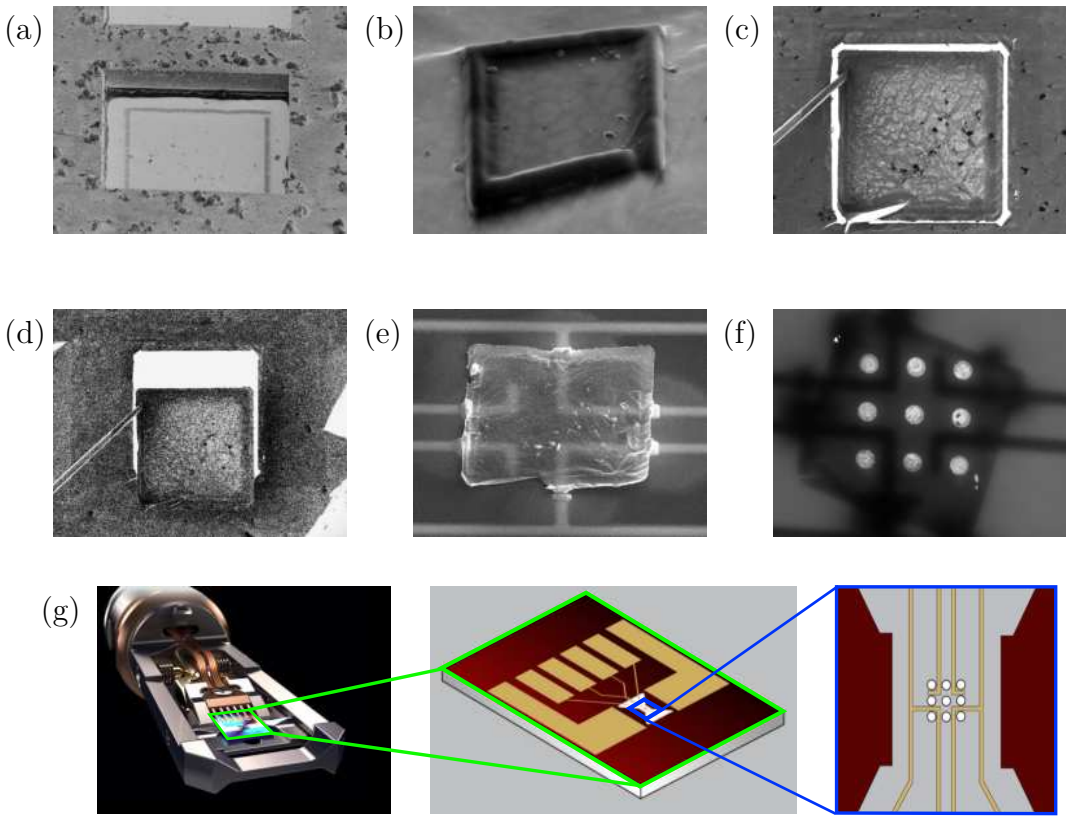

Figure 5.4: Fabrication process of a frame mounted on a MEMS chip. (a) E-beam predeposition of a protective cap. (b) I-beam deposition of the frame. (c) and (d) the cutting and lift-off of the frame. (e) SEM view of the frame positioned over the MEMS chip. (f) TEM view of the frame on attached to the MEMS chip. (g) Scheme of the electrothermal MEMS chip by Protochips.

Irradiation

In this section, we explain the ion dose dose quantification and FIB beam parameters.

When working with FIB, we first set the dimensions and shape of the pattern (6 × 6 μm square) we want to irradiate, then the accelerating voltage (30 kV) and ion current (1.1 pA). Those are the basic settings, which, however, produce very high ion doses (in order of 10^{15} or even higher). Hence, we have to delve into the advanced settings, which really allow us to shape the beam as needed. The most important parameters are the dwell time t_{D} and blur. Blur defines the diameter of the beam at the sample surface, and all other beam and spot size parameters (like pitch or overlap) are calculated from the set blur value. Dwell time is the time the beam "dwells" in one spot. As shown in Figure 5.5, scanning is not continuous, the pattern being irradiated is mathematically a grid with closely spaced spots. Those spots are spaced according to the pitch x and pitch y parameters, which are calculated from the blur value.

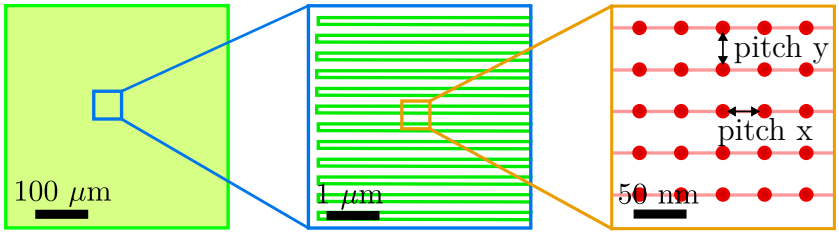

Figure 5.5: Scheme of FIB scanning. The ion beam scanning is not continuous, the pattern scanned is mathematically a grid with closely spaced spots. Those spots are spaced according to the pitch x and pitch y parameters, which are calculated from the blur value.

The dose can be then calculated as

$$D = \frac{It_{\mathrm{D}}}{p_{\mathrm{x}}p_{\mathrm{y}}e}N, \tag{5.2}$$

where I stands for the ion current, t_{D} is the dwell time, the parameters p_{x} and p_{y} stand for pitch in x and y direction, e stands for the elemental charge, as each Ga^{+} ion is ionized once and N stands for the number of passes the ion beam makes over the sample.